


# INDUSTRIAL CROPS AND PRODUCTS

AN INTERNATIONAL JOURNAL



☐  [Download selected articles](#) [Export](#)

☐ Research article ● *Open access*

1

## Service life prediction of chitosan-based self-healing coatings using four models and a neural network

EI检索

SCI升级版 农林科学1区

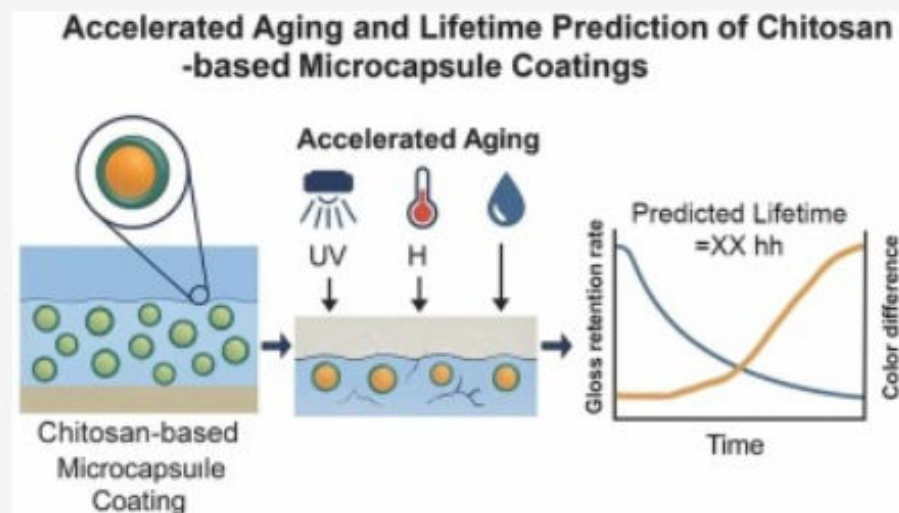
SCI基础版 农林科学1区

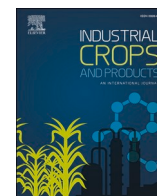
IF 6.2

*Industrial Crops and Products*, 1 April 2026

Yijuan Chang, Jinxin Wang, Zhihui Wu

 [View PDF](#) [Abstract](#) [Graphical Abstract](#) [Export](#)





# Service life prediction of chitosan-based self-healing coatings using four models and a neural network

Yijuan Chang<sup>a</sup>, Jinxin Wang<sup>a</sup>, Zhihui Wu<sup>a,b,\*</sup>

<sup>a</sup> College of Furnishings and Industrial Design, Nanjing Forestry University, Nanjing 210037, China

<sup>b</sup> Co-Innovation Center of Efficient Processing and Utilization of Forest Resources, Nanjing Forestry University, Nanjing 210037, China

## ARTICLE INFO

### Keywords:

Self-healing coating  
Color difference  
Gloss retention rate  
Neural network  
Lifespan predict

## ABSTRACT

Chitosan-based microencapsulation provides a sustainable approach for improving the durability of wood coatings; however, their resistance to coupled photo-thermal aging remains limited. In this study, three chitosan-derived microcapsule coating systems—chitosan-encapsulated wood wax oil (C-W), TiO<sub>2</sub>- and hydroxypropyl methylcellulose (HPMC)-modified chitosan-encapsulated wood wax oil (CTH-W), and TiO<sub>2</sub>- and HPMC-modified chitosan-encapsulated UV-curable wood wax oil (CTH-UVW)—were developed and systematically evaluated in terms of color stability, gloss retention, thermal behavior, structural degradation, and service-life prediction under accelerated photo-thermal aging. The results show that the synergistic incorporation of UV-curable wood wax oil with TiO<sub>2</sub>-reinforced and HPMC-densified capsule walls (CTH-UVW) significantly suppresses photo-oxidation and thermal degradation. At an optimal loading of 2.0 wt%, the CTH-UVW coating exhibited markedly extended color-difference lifetime (1310.6 h) and gloss-retention lifetime (493.6 h), outperforming both C-W and CTH-W systems. Service-life modeling revealed that neural network models provided the most accurate chromaticity predictions, whereas the Weibull model yielded the most reliable gloss-retention forecasts. Complementary analyses, including mass-loss measurements, thermogravimetric displacement, SEM observations, and FTIR spectroscopy, consistently confirmed that the CTH-UVW coating maintained the highest residual mass, minimal oxidation-related spectral changes, and the least surface cracking. Notably, the 2.0 wt% CTH-UVW coating retained the strongest adhesion after aging, indicating superior interfacial stability. This work demonstrates a synergistic microcapsule design that substantially extends coating service life, offering a sustainable and high-performance solution for long-term wood protection in outdoor and architectural applications.

## 1. Introduction

Wood coating is vulnerable to combined environmental stressors during long-term service (Gan et al., 2023; Wu et al., 2020; Zhou and Xu, 2024), including UV radiation (Wang et al., 2026), temperature-humidity fluctuations, and mechanical abrasion, which progressively degrade its structural and aesthetic integrity (Chen et al., 2022). Prolonged UV exposure accelerates photooxidation, polymer chain scission, and chromophore formation within the coating layer, while temperature and humidity cycling induces repeated swelling-shrinkage stresses that weaken interfacial adhesion and promote microcrack formation (Feng et al., 2025; Wang et al., 2023). Mechanical abrasion further disrupts the coating surface, creating localized defects that serve as initiation sites for deeper degradation. These stressors typically cause microcracking, gloss loss from surface roughening/microstructural

disorder (Dong et al., 2025a), and increased color difference due to pigment degradation, oxidation, and altered light reflection. and increased color difference resulting from pigment degradation, oxidation, and changes in light-reflective properties (Lin et al., 2024). To extend the service life of coatings while maintaining their decorative and protective functions (Slot et al., 2015), researchers have recently introduced microcapsule-based systems with self-healing capabilities (Bekas et al., 2016; Han et al., 2025). In these smart coatings, healing agents are encapsulated within polymeric or hybrid-shell microcapsules that remain dormant until the coating experiences mechanical damage (Deng et al., 2023). Upon the formation of microcracks, the propagating crack front ruptures the capsules, enabling the healing agents to flow into the damage zone, wet the crack surfaces, and polymerize or solidify to restore part of the coating's structural continuity, barrier function, and appearance (Li et al., 2018). This autonomous repair mechanism

\* Corresponding author at: College of Furnishings and Industrial Design, Nanjing Forestry University, Nanjing 210037, China.

E-mail addresses: [changyijuan@njfu.edu.cn](mailto:changyijuan@njfu.edu.cn) (Y. Chang), [wzh550@sina.com](mailto:wzh550@sina.com) (Z. Wu).

<https://doi.org/10.1016/j.indcrop.2026.123055>

Received 14 December 2025; Received in revised form 20 January 2026; Accepted 7 March 2026

Available online 12 March 2026

0926-6690/© 2026 The Authors. Published by Elsevier B.V. This is an open access article under the CC BY license (<http://creativecommons.org/licenses/by/4.0/>).

significantly reduces the rate of crack propagation and delays environmental deterioration. However, the service life of microcapsule-based coatings remains constrained by finite healing-agent reserves, UV/moisture-induced shell degradation, and the intrinsic aging of the polymer matrix under environmental stresses.

Given these limitations, service life prediction has become a critical aspect of evaluating the long-term performance of microcapsule-based coatings (Busso et al., 2007). Conventional prediction approaches—such as power-law and Arrhenius models (Croll and Hinderliter, 2008)—primarily rely on accelerated aging data and empirical fitting procedures (Gribova et al., 2021; Šušteršič et al., 2023; Traeger et al., 2003). However, these methods often struggle to accurately capture the nonlinear, multi-factor-coupled degradation behavior that occurs under realistic environmental exposure. Appearance-related indicators, particularly color difference and gloss retention, are strongly influenced by the combined effects of UV radiation, humidity, temperature fluctuations, and the time-dependent release behavior of microcapsules, making it difficult for single empirical models to achieve high prediction accuracy. These challenges highlight the need for more advanced predictive frameworks capable of describing the complex degradation patterns observed in smart coating systems.

With the advancement of artificial intelligence, neural network-based methods have emerged as promising tools for coating lifetime prediction due to their strong nonlinear mapping and pattern-recognition capabilities (Li et al., 2025; Taskinen and Yliruusi, 2003). Neural networks can integrate multidimensional input variables, learn hidden degradation mechanisms, and provide robust predictive performance without requiring predefined mathematical expressions. In this study, a neural network model was constructed using experimental data on color difference, gloss retention, and environmental parameters (Dong et al., 2025b; Kriegeskorte and Golan, 2019). Its predictive accuracy was systematically compared with traditional lifetime models, including the power-law (Clauaset et al., 2009), exponential (Li et al., 2015), Weibull (Prabhakar Murthy et al., 2004; Smith, 1991), and Avrami (Jonas et al., 2009) models, to identify the most suitable model for accurate lifetime prediction of microcapsule coatings. This approach not only deepens the mechanistic understanding of their durability but also provides a reliable theoretical and design basis for the engineering application of wood-based materials.

## 2. Materials and methods

### 2.1. Materials

*Fagus sylvatica* board, 5 cm × 5 cm, 90 pieces. UV topcoat, composed of epoxy acrylic resin, polyester acrylic resin, low molecular weight acrylate reactive diluents (including tripropylene glycol diacrylate (TPGDA) and trimethylolpropane triacrylate (TMPTA)), photoinitiator, defoaming agent, and leveling agent, was provided by Jiangsu Haitian Technology Co., wood wax oil (WWO), UV wood wax oil (UVW), chitosan coated wood wax oil (C-W microcapsules), hydroxypropyl methylcellulose-modified chitosan TiO<sub>2</sub>-coated wood wax oil microcapsules (CTH-W microcapsules), hydroxypropyl methylcellulose-modified chitosan TiO<sub>2</sub>-coated UV wood wax oil (CTH-UVW microcapsules), 30 μm wire rods, AB glue. UV lamp with a wavelength of 276 nm. The wood wax oil and UV wood wax oil used in this study were synthesized according to our previously reported methods (Chang and Wu, 2024). Briefly, the wood wax oil was obtained by the photoinitiated modification of thistle oil and linseed oil, while the UVW was prepared by incorporating Irgacure 2959 as a photoinitiator to achieve rapid UV curing. The detailed synthesis procedures and characterization results (e.g., FTIR, viscosity, and photopolymerization behavior) have been described in our previous publication.

### 2.2. Self-healing microcapsule preparation

Three types of microcapsules were prepared based on our previously reported method (Chang et al., 2024), with modifications in the core or shell components to achieve different release behaviors. Specifically, the C-W microcapsules employed WWO as the core material, exhibiting an average particle size of 3–5 μm and an encapsulation efficiency of 73.7%. The CTH-W microcapsule incorporated HPMC and TiO<sub>2</sub>-modified chitosan as the shell (Chang et al., 2025), with an average particle size of 2–3 μm and an encapsulation efficiency of 95.6%. The CTH-UVW microcapsules were prepared with UVW as the encapsulated core, achieving an average particle size of 6–7 μm and an encapsulation efficiency of 78.2%. Detailed synthesis procedures are available in our previous publication. The average particle size, morphology, and encapsulation efficiency of the microcapsules were consistent with those reported previously.

### 2.3. Microcapsule coating preparation

The C-W, CTH-W, and CTH-UVW microcapsule coatings were each formulated by blending the corresponding microcapsules with UV-curable coating at loadings of 1 wt%, 2 wt%, and 3 wt%, respectively. The mixtures were stirred thoroughly to ensure uniform dispersion of the microcapsules. The coatings were then applied onto *Fagus sylvatica* substrates using a 30 μm wire bar and subsequently cured under UV irradiation for 30 s.

### 2.4. Accelerated aging test

The weathering performance of the microcapsule coatings applied to the *Fagus sylvatica* substrates surface was evaluated in accordance with GB/T 1865–2009. To better approximate real service environments, a multi-factor alternating aging protocol was employed. UV aging was performed using UVB-340 fluorescent lamps at an irradiance of 0.55 W/m<sup>2</sup>. Each aging cycle consisted of 4 h of UV exposure at 60 °C followed by 4 h of condensation at 50 °C with a relative humidity of 99%.

### 2.5. Optical performance

**Color difference.** The chromaticity value measurements were performed on *Fagus sylvatica* substrates using a SEGT-J portable colorimeter (Zhuhai Tianchuang Instrument Co., Ltd., Zhuhai, China). The color parameters L<sub>1</sub>, a<sub>1</sub>, b<sub>1</sub> corresponded to the reference (blank) samples, while L<sub>2</sub>, a<sub>2</sub>, b<sub>2</sub> represented the treated samples. Here, L denotes lightness, a represents the chromatic coordinate ranging from red to green, and b represents the coordinate ranging from blue to yellow. The color difference (ΔE) was calculated according to the following equation (Coronel-Aguilera and San Martín-González, 2015) (1):

$$\text{Color difference } (\Delta E) = [(\Delta L^*)^2 + (\Delta a^*)^2 + (\Delta b^*)^2]^{1/2} \quad (1)$$

where  $\Delta L^* = L_1 - L_2$ ,  $\Delta a^* = a_1 - a_2$ , and  $\Delta b^* = b_1 - b_2$

**Gloss.** The self-healing microcapsule coating was applied onto 50 mm × 50 mm *Fagus sylvatica* substrates, and the gloss of the coating at 85° angle was measured using an HG268 intelligent gloss meter (3nh Technology Co., Ltd., Shenzhen) in accordance with the GB/T 4893.6–2013 “Furniture Surface Coating Physicochemical Properties Testing—Part 6: Gloss Measurement Method.” The gloss retention ratio as defined in Eq. (2), was used to evaluate the relative preservation of surface gloss during the aging process.

$$\text{GR} = \frac{G_t}{G_0} \times 100\% \quad (2)$$

GR is the Gloss retention rate, G<sub>0</sub> is the gloss before aging, and G<sub>t</sub> is the gloss after aging.

Chromaticity and gloss were recorded every 8 h throughout the



496 h exposure period.

## 2.6. Adhesion strength

The adhesion between the coating and the wood substrate was evaluated according to the ASTM D4541–02 standard using a BEVS 2201 pull-off adhesion tester. The coating surface on the substrate and the 10 mm diameter steel dolly were abraded with 1000-grit sandpaper and subsequently cleaned with ethanol to remove grease and dust. A low-odor acrylic AB adhesive (Leaftop, China) was thoroughly mixed and uniformly applied onto the coated wood surface. The steel dolly was then pressed onto the adhesive layer, and any excess adhesive was carefully removed using a cotton swab. After curing for 24 h at ambient conditions, the pull-off test was performed. Three parallel specimens were tested for each coating type, and the average adhesion strength was recorded. The pull-off rate was set to 0.8 MPa/s, followed by maintaining a holding pressure of 10 MPa for 10 s. The aging adhesion strength was tested at 100 h, 200 h, and 496 h, respectively.

## 2.7. Thermal stability

Thermogravimetric (TG) analysis measurements of microcapsule UV coatings were performed on a TG 209 from TA Instruments to study the thermal stability of the coating before and after aging. The temperature ramp was maintained at a controlled rate of 10 °C/min with a flow rate of 20 mL/min, within a heating range spanning from room temperature to 700 °C.

## 2.8. Microscopic test

The microscopic morphology of the microcapsules coatings was observed using Zeiss microscope and Quanta-200 scanning electron microscope (SEM). The functional group variations of the coatings before and after aging were analyzed using a VERTEX 80 V Fourier transform infrared (FTIR) spectrometer (Bruker, Germany) equipped with an attenuated total reflectance (ATR) accessory. X-ray photoelectron spectroscopy (XPS) was performed on AXIS UltraDLD model equipment sourced from Shimadzu Corporation Japan featuring power output set at 600 W alongside resolution capabilities exceeding 3 μm which facilitated the acquisition of chemical energy spectra about aerogel samples analyzed herein.

## 2.9. Coating service life prediction models

A comparative analysis was conducted using five models—the power law, exponential, Weibull, Avrami, and neural network models—to identify the most suitable model for predicting the aging behavior of microcapsule-based coatings. In the modeling process, aging time was set as the independent variable, while color difference and gloss retention were used as dependent variables. Critical performance thresholds were defined as a color difference ( $\Delta E$ ) greater than 10 and a gloss retention ratio reduced to 50.0%. The predicted service life obtained from each model was compared with the experimental data to verify model reliability. Model parameters were further refined using natural aging data to enhance prediction accuracy. The resulting curves described the evolution of coating properties over aging time, and a lifetime prediction equation for self-healing microcapsule coatings was proposed, providing a theoretical basis for optimizing microcapsule formulations (e.g., wall thickness and core material content).

The power law model (Lux and Alfarano, 2016), as expressed in Eq. (3), describes the variation of the performance parameter (color difference) with aging time  $t$  as follows:

$$\Delta E(t) = a \cdot t^{-n} \quad (3)$$

Here,  $a$  represents the initial performance value at  $t = 1$ , and  $n$  denotes the degradation index, which reflects the rate of deterioration ( $a$

decrease in performance over time when  $n > 0$ ). This model captures the complex degradation behavior resulting from the synergistic effects of moisture, heat, and mechanical wear.

The gloss lifetime is defined as the time point at which the gloss retention rate drops to 50%. Therefore, a power-law model (4) can be used to fit the gloss lifetime, and the specific calculation is shown in Eq. (5):

$$GR(t) = A \cdot t^{-n} \quad (4)$$

$$\log(GR) = \log A - n \log t \quad (5)$$

The exponential model is shown in formula (Bloomfield, 1973) (6).

$$y = a \cdot e^{b \cdot t} \quad (6)$$

In this model,  $a$  represents the initial value, corresponding to the gloss retention ratio at  $t = 0$ ,  $e$  is the natural constant (approximately 2.718),  $b$  is the exponential decay coefficient ( $b < 0$ ), and  $t$  denotes the aging time.

The Weibull model is shown in Eq. (7) (Wais, 2017).

$$y = a \cdot e^{-(t/b)^c} \quad (7)$$

where  $a$  denotes the initial value, corresponding to the gloss retention ratio at  $t = 0$ ,  $b$  is the characteristic lifetime parameter, representing the time at which the system undergoes approximately 50.0% degradation, and  $c$  is the shape parameter that defines the curvature of the degradation profile.

The degradation kinetics of the coating were further described using the Avrami model (Shirzad and Viney, 2023), as presented in Eq. (8).

$$y = a \cdot e^{-kt^n} \quad (8)$$

where  $a$  represents the initial value, corresponding to the gloss retention ratio at  $t = 0$ ,  $K$  is the rate constant; and  $n$  denotes the reaction exponent.

In addition to empirical kinetic models, a feedforward artificial neural network was employed to capture the nonlinear relationship between color difference ( $\Delta E$ ) and aging time. The neural network was implemented using a multilayer perceptron (MLP) architecture with one input neuron representing exposure time, two hidden layers each containing 50 neurons, and one output neuron corresponding to  $\Delta E$ . Rectified Linear Unit (ReLU) activation functions were applied in the hidden layers, and the network was optimized using the Adam algorithm with a maximum of 5000 training iterations. Prior to training, both input and output variables were standardized using Z-score normalization to improve numerical stability and convergence. Model training was performed on the full experimental dataset, and the predicted outputs were subsequently transformed back to the original scale. The coefficient of determination ( $R^2$ ) was calculated to evaluate fitting performance. The service life was estimated by scanning the trained neural network over an extended time range and identifying the time point at which the predicted color difference first exceeded the failure threshold ( $\Delta E = 10$ ), consistent with the criterion applied to conventional kinetic models. Given the limited number of experimental data points available from accelerated aging tests, the neural network was primarily employed as a flexible nonlinear fitting tool rather than a purely predictive model. Therefore, the full dataset was used for training to enable a fair comparison with conventional empirical models, which were also fitted to the same data range.

To model the degradation behavior of gloss retention during accelerated aging, a feedforward artificial neural network was employed as a data-driven nonlinear regression approach. The neural network was implemented using a multilayer perceptron architecture with one input neuron representing aging time, three hidden layers consisting of 64, 32, and 16 neurons, respectively, and one output neuron corresponding to gloss retention (%). Hyperbolic tangent (tanh) activation functions were applied in all hidden layers to ensure smooth monotonic decay behavior consistent with physical degradation processes. Prior to training, both

input and output variables were normalized using Z-score standardization. The network was trained using the Adam optimization algorithm with an initial learning rate of 0.0005 and an L2 regularization coefficient of  $1 \times 10^{-4}$ . Early stopping was employed to prevent overfitting, with 15% of the dataset automatically reserved as a validation set during training. Training was terminated when the validation error failed to improve for 100 consecutive iterations, with a maximum of 20,000 iterations allowed. A fixed random seed was used to ensure reproducibility. To suppress minor numerical oscillations in the predicted degradation curve, the neural network outputs were further smoothed using a Savitzky–Golay filter (window length = 7, polynomial order = 2), followed by a slight amplitude correction. The gloss service life was determined as the time at which the predicted gloss retention first decreased below 50%, consistent with the failure criterion applied to empirical kinetic models.

### 3. Results and discussion

#### 3.1. Aging resistant optical performance

The color difference and gloss retention of the three types of microcapsule-based coatings before and after accelerated aging are presented in Fig. 1. For the neat UV coating,  $\Delta E$  increased progressively with aging time (Fig. 1a), which was attributable to photooxidation and chromophore formation within the UV-cured polymer network (e.g., carbonyl- and conjugation-containing species) as well as gradual surface roughening that altered light scattering. After incorporation of C–W microcapsules, whose core consisted of WWO dominated by long-chain (partly unsaturated) fatty-acid derivatives, the rate of  $\Delta E$  increase became dependent on microcapsule loading. In particular, the 3% C–W coating exhibited the fastest color change, indicating that a higher content of oil-filled capsules promoted color instability during aging. This behavior was consistent with the susceptibility of unsaturated oil constituents to photooxidation; hydroperoxide formation/

decomposition and subsequent chain scission can yield colored secondary oxidation products and low-molecular-weight species that may migrate to the surface, thereby accelerating discoloration. Meanwhile, at low loading (1% C–W), the amount of microcapsules was likely insufficient to provide effective buffering and defect-healing throughout the coating, resulting in a relatively high  $\Delta E$ . For the CTH–W coatings (Fig. 1b), the same WWO core was encapsulated within a chitosan/HPMC/TiO<sub>2</sub> hybrid shell. Compared with the C–W system, all CTH–W coatings exhibited markedly lower  $\Delta E$  values and a more uniform increase across different loadings, suggesting that the wall composition exerted a dominant influence on color stability. The improved performance was attributed to (i) the TiO<sub>2</sub>-containing shell providing enhanced UV shielding and thereby reducing the photochemical conversion of both the UV matrix and the oil core, and (ii) the polysaccharide-rich wall (chitosan/HPMC) acting as a diffusion/transport barrier that limited oxygen and radical ingress as well as the outward migration of oil-derived oxidation products. Nevertheless, the more rapid  $\Delta E$  increase observed for the 3% CTH–W coating after 300 h implied that, beyond prolonged exposure, the protective function of the shell could be partially compromised (e.g., by surface erosion and microdefect accumulation), allowing increased photooxidation and/or migration of degradation products. In the CTH–UVW system (Fig. 1c), the capsule wall remained chitosan/HPMC/TiO<sub>2</sub>, whereas the core consisted of a UVW rather than unreacted oil. The UVW forms a more constrained and denser network, which could in turn suppress the release and surface migration of chromophoric low-molecular-weight products. Accordingly, the 2% CTH–UVW coating exhibited the smallest increase in  $\Delta E$  throughout aging, indicating an optimal balance between microcapsule availability for damage buffering/self-healing and the preservation of optical stability. By contrast, 3% CTH–UVW showed the largest long-term  $\Delta E$  increase, likely due to interfacial-density-driven heterogeneities (agglomeration/voids/roughness) that increased scattering and promoted localized degradation. Overall, the results indicated that discoloration was governed by the combined

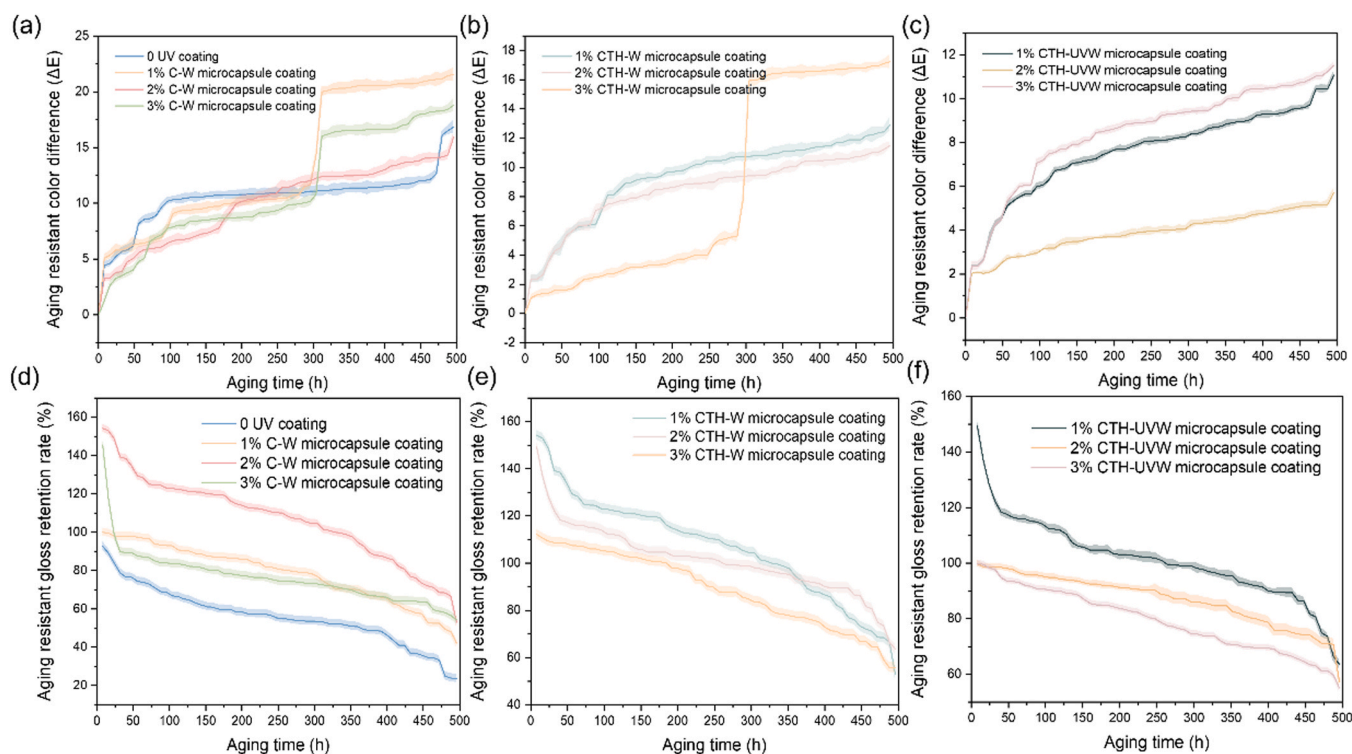


**Fig. 1.** Color difference and gloss retention rate after aging of microcapsule coating: (a) color difference of pure UV coating and C–W microcapsule coating, (b) color difference of CTH–W microcapsule coating, (c) color difference of CTH–UVW microcapsule coating, (d) gloss retention rate of pure UV coating and C–W microcapsule coating, (e) gloss retention rate of CTH–W microcapsule coating, (f) gloss retention rate of CTH–UVW microcapsule coating.

effects of (i) the photochemical susceptibility of the core, (ii) the UV-shielding and barrier properties imparted by the chitosan/HPMC/TiO<sub>2</sub> shell, and (iii) microcapsule-loading-induced changes in coating heterogeneity and surface scattering. Among all formulations, the 2% CTH-UVW coating provided the best aging resistance, maintaining the lowest  $\Delta E$  growth over the entire exposure period.

As shown in Fig. (d–f), the aging-resistant gloss retention rate decreased continuously with exposure time for all coatings, whereas the magnitude and decay rate strongly depended on the microcapsule design (core/shell chemistry) and loading. For the C–W microcapsule coating, the neat UV coating exhibited the lowest gloss retention throughout aging, while microcapsule addition improved gloss retention and produced a clear optimum at 2.0 wt%: the 2% C–W coating maintained the highest gloss retention over the entire period, whereas the 1% and 3% C–W coatings showed intermediate performance. This trend was attributed to the WWO core, which was rich in long-chain aliphatic (partly unsaturated) constituents and could be released to smooth microdefects and partially compensate for aging-induced surface roughening. At 1% capsule loading, the buffering/self-smoothing effect was insufficient, whereas 3% loading increased interfacial defects and oil-related surface inhomogeneity, enhancing light scattering and accelerating gloss loss. For the CTH–W coatings, in which the same WWO core was encapsulated by a chitosan/HPMC/TiO<sub>2</sub> hybrid wall, a more consistent and generally higher gloss retention was observed, with the performance ranking of 1% > 2% > 3% across aging times. The improved retention was consistent with the barrier function of the polysaccharide wall (restricting oxygen/water ingress and outward migration of mobile species) together with UV shielding from TiO<sub>2</sub>, both of which mitigated surface chalking and roughening. A similar loading trend occurred in CTH–UVW (1% > 2% > 3%), with UVW providing extra stabilization by forming a denser UV-cured network that limits oil exudation/blooming and thus reduces surface film inhomogeneity and light scattering. Overall, the gloss-retention curves indicated that

optimal microcapsule loading was required to balance defect-buffering/self-healing benefits against interface-induced heterogeneity. Accordingly, the best gloss retention was achieved at 2% for C–W and at 1% for both CTH–W and CTH–UVW, whereas excessive loading (3%) consistently accelerated gloss degradation during prolonged aging.

### 3.2. Optical lifetime prediction

The color difference lifetime of the pure UV coating and the C–W microcapsule-modified coatings is shown in Fig. 2. As presented in Fig. 2(a), the predicted color difference lifetime of the pure UV coating is 92.3 h. The fitting coefficients ( $R^2$ ) of the power law, exponential, Weibull, and Avrami models are all above 0.7, while the neural network model achieves the highest fitting accuracy with  $R^2 = 0.954$ , indicating superior reliability of the prediction. In Fig. 2(b), the color difference lifetime of the 1.0 wt% C–W microcapsule coating predicted by the neural network model is 193.5 h. Among the four conventional models, the exponential model gives  $R^2 = 0.876$ , and both the Weibull and Avrami models show  $R^2 = 0.819$ , which are notably lower than the neural network model ( $R^2 = 0.951$ ). As shown in Fig. 2(c), the 2.0 wt% C–W microcapsule coating exhibits a predicted lifetime of 193.5 h. The fitting coefficients for the power law, exponential, Weibull, and Avrami models are 0.860, 0.876, and 0.819, respectively, while the neural network again provides the highest accuracy ( $R^2 = 0.951$ ). In Fig. 2(d), the 3.0 wt% C–W microcapsule coating displays a predicted lifetime of 209.5 h. The power law model achieves a high fitting accuracy ( $R^2 = 0.988$ ), followed by the Weibull and Avrami models ( $R^2 = 0.985$ ), whereas the exponential model yields a much lower correlation ( $R^2 = 0.757$ ). Overall, these results demonstrate that the incorporation of C–W microcapsules effectively enhances the color difference lifetime of the coating. The 2.0 wt% C–W microcapsule formulation exhibits the longest service life, whereas both higher and lower microcapsule loadings tend to reduce the durability of the UV coating.

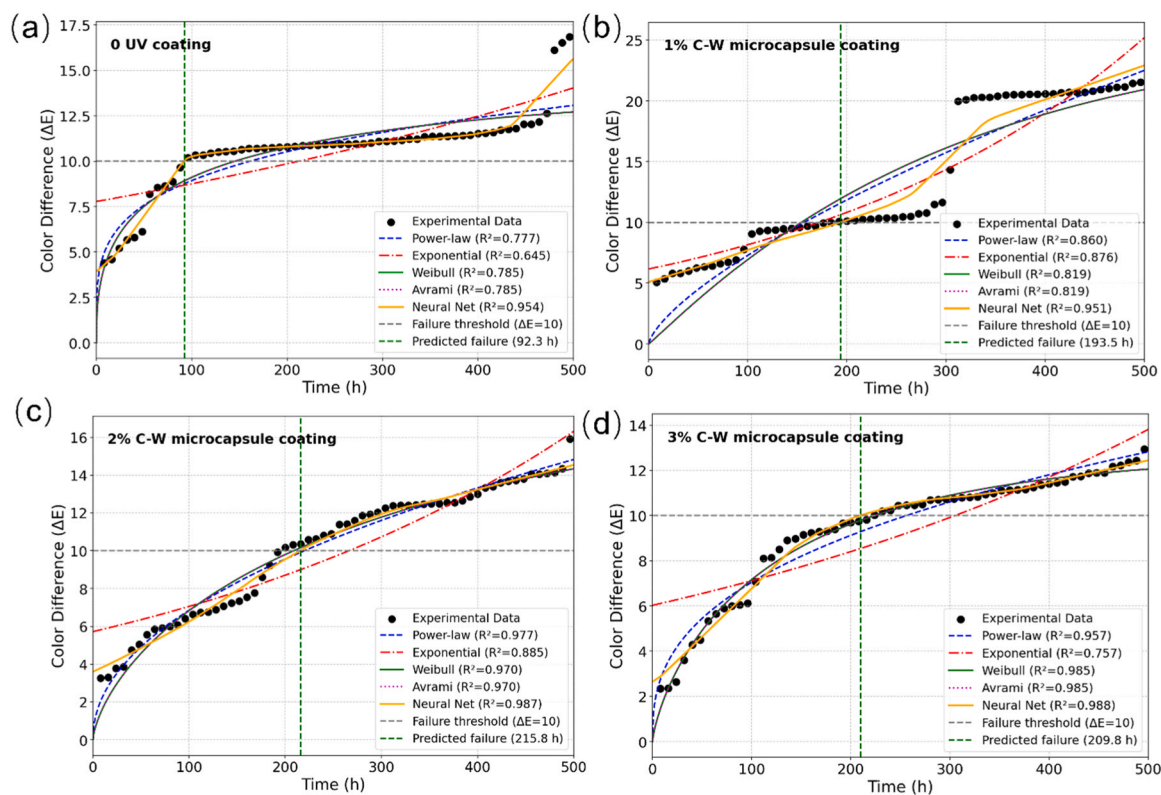


**Fig. 2.** Prediction of color difference life of UV coating and C-W microcapsule coating: (a) Pure UV coating, (b) 1.0% C-W microcapsule UV coating, (c) 2.0% C-W microcapsule UV coating, (d) 3.0% C-W microcapsule UV coating.



The lifespan prediction of the CTH-W microcapsule coatings is presented in Fig. 3. As shown in Fig. 3(a), the predicted lifespan of the coating containing 1.0 wt% microcapsules was 215.8 h. The power-law model exhibited a goodness of fit ( $R^2$ ) is 0.977, while both the Weibull and Avrami models yielded  $R^2$  values of 0.970, indicating satisfactory fitting performance. The neural network model was identified as the optimal model. As shown in Fig. 3(b), the predicted lifespan of the coating containing 2.0 wt% microcapsules was 337.8 h. The exponential model showed a relatively low  $R^2$  of 0.786, whereas the Weibull and Avrami models both achieved  $R^2$  values of 0.985, and the neural network model exhibited the highest fitting accuracy with an  $R^2$  of 0.986, suggesting reliable prediction results. In Fig. 3(c), the predicted lifespan of the coating containing 3.0 wt% microcapsules was 293.7 h. The Weibull model yielded an  $R^2$  of 0.916, while the remaining three models all exhibited  $R^2$  values greater than 0.8, confirming good agreement between experimental and predicted data. With the increase of microcapsule content from 1 wt% to 3 wt%, the predicted lifespan first increased and then decreased. This trend suggested that excessive microcapsule loading accelerated color degradation and reduced the anti-aging performance of the coating. At higher microcapsule concentrations, particle aggregation likely occurred, leading to the formation of micropores or interfacial defects that facilitated the diffusion of moisture and oxygen into the coating interior, thereby accelerating the aging process.

The color-difference lifetime prediction for CTH-UVW microcapsule coatings is shown in Fig. 4. As shown in Fig. 4(a), the predicted lifetime of the coating containing 1.0 wt% microcapsules was 442.5 h. The power-law model ( $R^2 = 0.906$ ) and both Weibull and Avrami models ( $R^2 = 0.884$ ) exhibited moderate fitting accuracy, whereas the neural network model achieved the highest correlation ( $R^2 = 0.991$ ), indicating superior predictive reliability. In Fig. 4(b), the coating with 2.0 wt% microcapsules showed a significantly extended lifetime of 1310.6 h. The exponential model yielded an  $R^2$  of 0.920, while the other three

empirical models all exceeded  $R^2 > 0.8$ . Again, the neural network exhibited the best performance with  $R^2 = 0.941$ . As shown in Fig. 4(c), the coating containing 3.0 wt% microcapsules presented a predicted color difference lifetime of 502.5 h, with the power-law, weibull, and avrami models all reaching  $R^2 > 0.9$ , suggesting satisfactory simulation accuracy. Overall, the incorporation of 2.0 wt% CTH-UVW microcapsules remarkably enhanced the coating's anti-aging ability, imparting excellent color stability during prolonged exposure.

Gloss retention rate lifetime prediction of UV and C-W microcapsule coatings is presented in Fig. 5. All samples exhibited a gradual decline in gloss retention rate with increasing aging time. As shown in Fig. 5(a), the pure UV coating exhibited a predicted lifetime of 359.1 h based on the neural network model, which achieved the highest correlation ( $R^2 = 0.984$ ), indicating that the unmodified coating still possessed a certain degree of durability. The power-law model was unsuitable for predicting gloss retention in this case, whereas the exponential, weibull, and avrami models all demonstrated satisfactory fits ( $R^2 = 0.916$ ). In Fig. 5(b), the coating containing 1.0 wt% C-W microcapsules showed a predicted lifetime of 493.6 h, with the neural network model yielding a strong correlation ( $R^2 = 0.983$ ). In contrast, the power-law model presented a poor fit ( $R^2 = 0.501$ ), suggesting its inapplicability for gloss prediction. The exponential, weibull, and avrami models all exhibited  $R^2 > 0.9$ , confirming the reliability of the prediction. As shown in Fig. 5(c), the 2.0 wt% C-W microcapsule coating exhibited a lifetime of 547 h, with the neural network model achieving  $R^2 = 0.976$ , while both the Weibull and Avrami models provided good fits ( $R^2 > 0.9$ ). The power-law model, however, yielded a much lower correlation ( $R^2 = 0.620$ ), indicating that it was unsuitable for this dataset. For the 3.0 wt% C-W microcapsule coating (Fig. 5d), the predicted lifetime was 546.6 h using the neural network model, with  $R^2 = 0.895$  for the power-law model,  $R^2 = 0.734$  for the exponential model, and  $R^2 = 0.869$  for both Weibull and Avrami models, reflecting reasonable prediction accuracy. Overall, the incorporation of 2.0 wt% C-W microcapsules provided the most stable

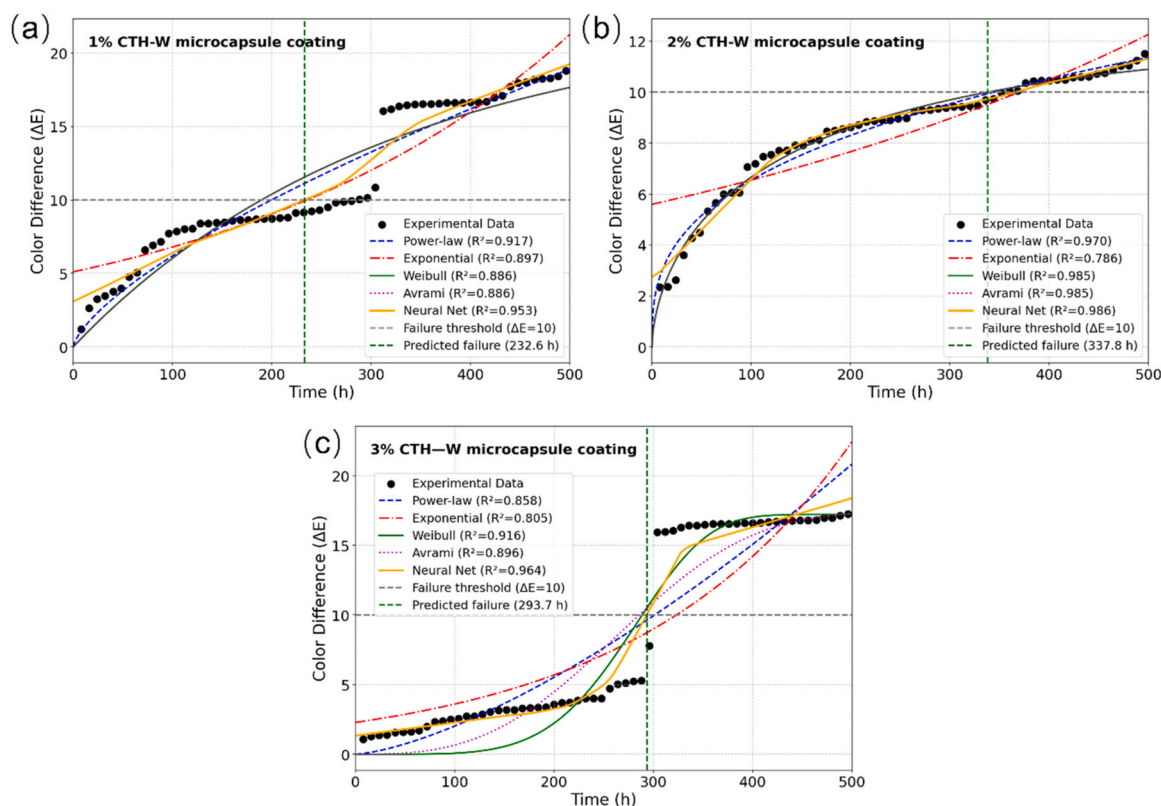
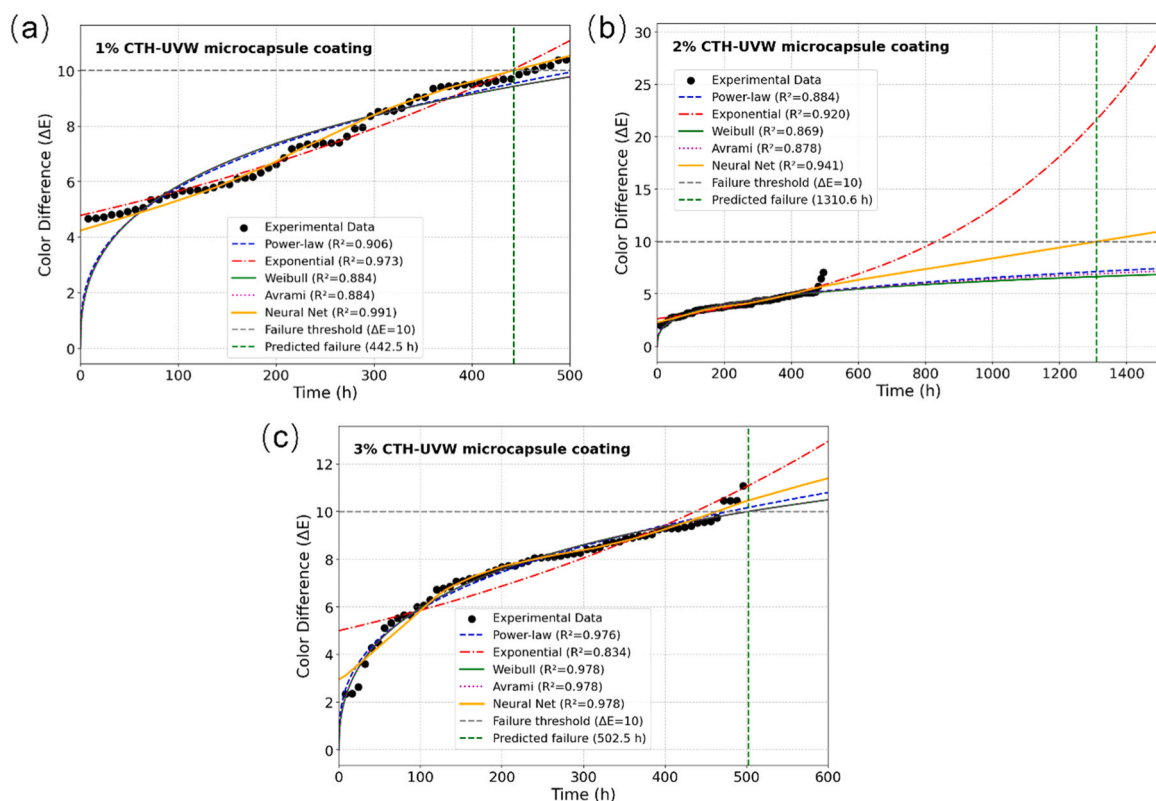
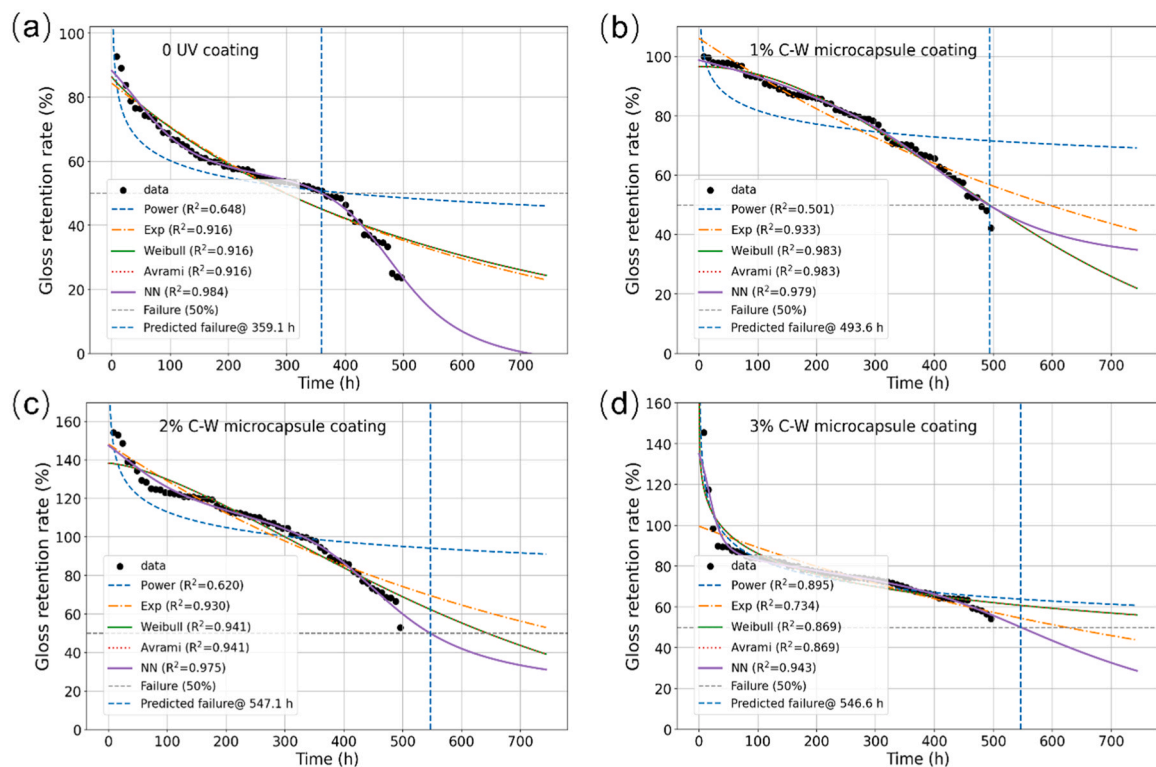


Fig. 3. Prediction of color difference life of CTH-W microcapsule UV coating: (a) 1.0% CTH-W microcapsule coating, (b) 2.0% CTH-W microcapsule coating, (c) 3.0% CTH-W microcapsule coating.





**Fig. 4.** Prediction of color difference lifetime of CTH-UVW microcapsule UV coating: (a) 1.0% CTH-UVW microcapsule coating, (b) 2.0% CTH-UVW microcapsule coating, (c) 3.0% CTH-UVW microcapsule coating.



**Fig. 5.** Gloss lifespan prediction of UV coatings: (a) pure UV coating, (b) 1.0% C-W microcapsule UV coating, (c) 2.0% C-W microcapsule UV coating, and (d) 3.0% C-W microcapsule UV coating.

gloss retention, while excessive or insufficient microcapsule content accelerated coating degradation, underscoring the importance of

optimizing microcapsule concentration for enhanced durability.

The gloss retention lifetime prediction of CTH-W microcapsule coatings is illustrated in Fig. 6. As shown in Fig. 6(a), the coating containing 1.0% microcapsules exhibited a predicted gloss lifetime of 607.2 h based on the weibull model, which provided the best fitting performance. In contrast, the power-law model yielded a poor correlation ( $R^2 = 0.467$ ), indicating its unsuitability for this dataset. In Fig. 6(b), the coating with 2.0% microcapsules achieved a weibull predicted lifetime of 569.5 h, while the power-law model again showed low fitting accuracy ( $R^2 = 0.571$ ), demonstrating limited predictive reliability. The gloss retention lifetime at this concentration increased by more than twofold compared with the 1.0% microcapsule coating, highlighting a clear enhancement in aging resistance. As shown in Fig. 6(c), the 3.0% microcapsule coating exhibited a predicted gloss lifetime of 574.9 h. The experimental, weibull, and avrami models all showed high coefficients of determination ( $R^2 > 0.9$ ), while the power-law model displayed poor fitting performance ( $R^2 = 0.523$ ), confirming that it is unsuitable for predicting the gloss lifetime of CTH-W microcapsule coatings. The superior gloss retention observed for the 1.0% CTH-W microcapsule coating can be attributed to the self-healing behavior under UV or hydrothermal conditions. Partial rupture of the microcapsules releases liquid WWO, which migrates into microcracks or roughened regions, forming a renewed smooth surface that enhances specular reflection and gloss. When the microcapsule content is too low, the released core material is insufficient to maintain the UV coating integrity. Conversely, excessive microcapsule loading compromises the structural compactness of the coating.

Gloss retention lifetime prediction of CTH-UVW microcapsule coatings is shown in Fig. 7. As presented in Fig. 7(a), the 1.0 wt% microcapsule coating exhibited a predicted gloss retention lifetime of 569.5 h using the neural network model, which achieved the highest correlation ( $R^2 = 0.942$ ), indicating its superior fitting performance in nonlinear regions. Other models showed relatively poor correlations, reflecting significant divergence among the four empirical approaches.

The pronounced differences suggest high model sensitivity during extrapolation. Notably, the weibull and neural network predictions aligned more closely with the experimental trend, while the avrami model clearly overestimated the lifetime. As shown in Fig. 7(b), the 2.0 wt% microcapsule coating demonstrated a predicted lifetime of 665.7 h based on the weibull model. The power-law model exhibited a low correlation ( $R^2 = 0.571$ ), indicating poor predictive capability. In contrast, the weibull and avrami models displayed strong consistency and closely matched the decaying trend of the experimental data. The neural network model performed reasonably well but showed slightly reduced robustness under extrapolated conditions. For the 3.0 wt% microcapsule coating (Fig. 7c), the predicted gloss retention lifetime reached 660.7 h, with both the weibull and avrami models achieving  $R^2 = 0.989$ , markedly outperforming the power-law model. The exponential model also exhibited excellent accuracy ( $R^2=0.986$ ), while the neural network model achieved  $R^2 = 0.955$ , demonstrating strong capability to capture the degradation behavior despite minor deviations at extended aging times.

A notable distinction was observed in the predictive performance of different models: the neural network exhibited superior accuracy in  $\Delta E$  prediction, whereas the Weibull model demonstrated greater robustness in gloss retention prediction. This divergence can be rationalized by considering the underlying aging mechanisms governing each performance metric. Color change is typically governed by multiple concurrent and highly nonlinear processes, including photo-oxidation, chromophore formation, pigment degradation, and moisture-assisted chemical reactions. These complex, coupled effects are difficult to capture with predefined parametric equations but are well suited to data-driven approaches such as neural networks, which can learn nonlinear patterns directly from experimental data. In contrast, gloss degradation is predominantly associated with more monotonic and cumulative physical-chemical processes, such as surface roughening, microcrack development, and progressive oxidation of the polymer matrix. These processes often exhibit a gradual, irreversible decay behavior with time,

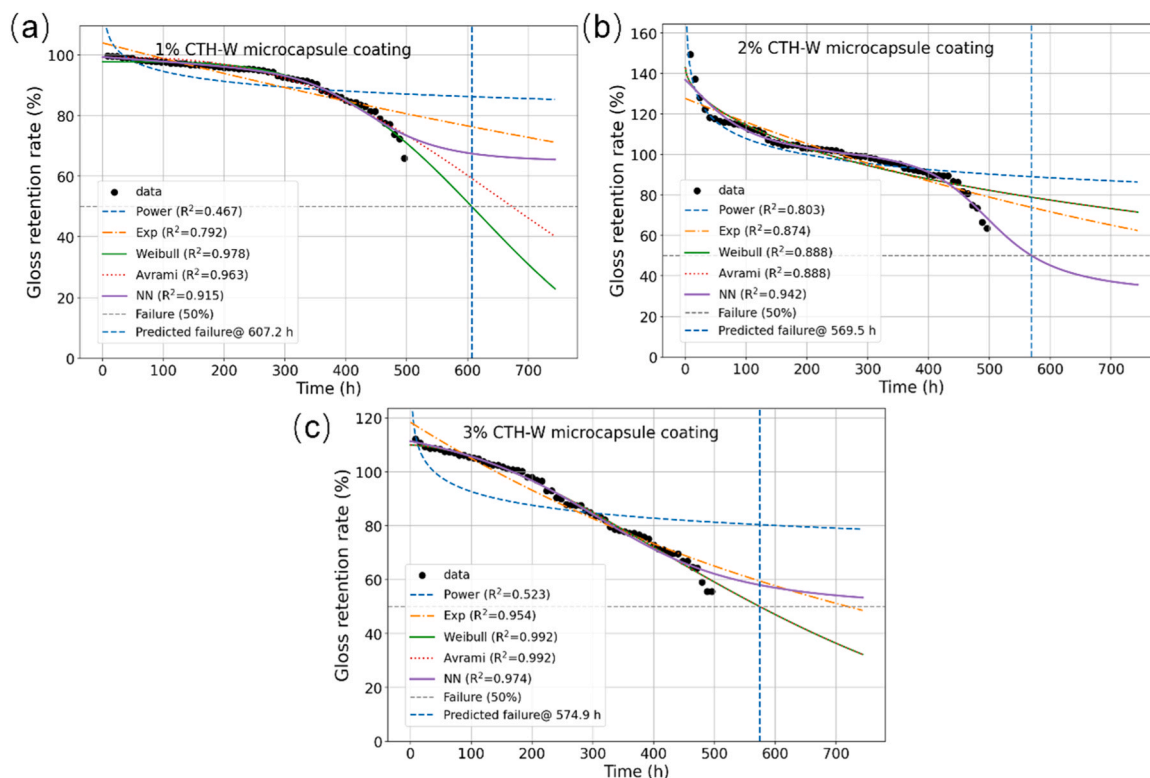
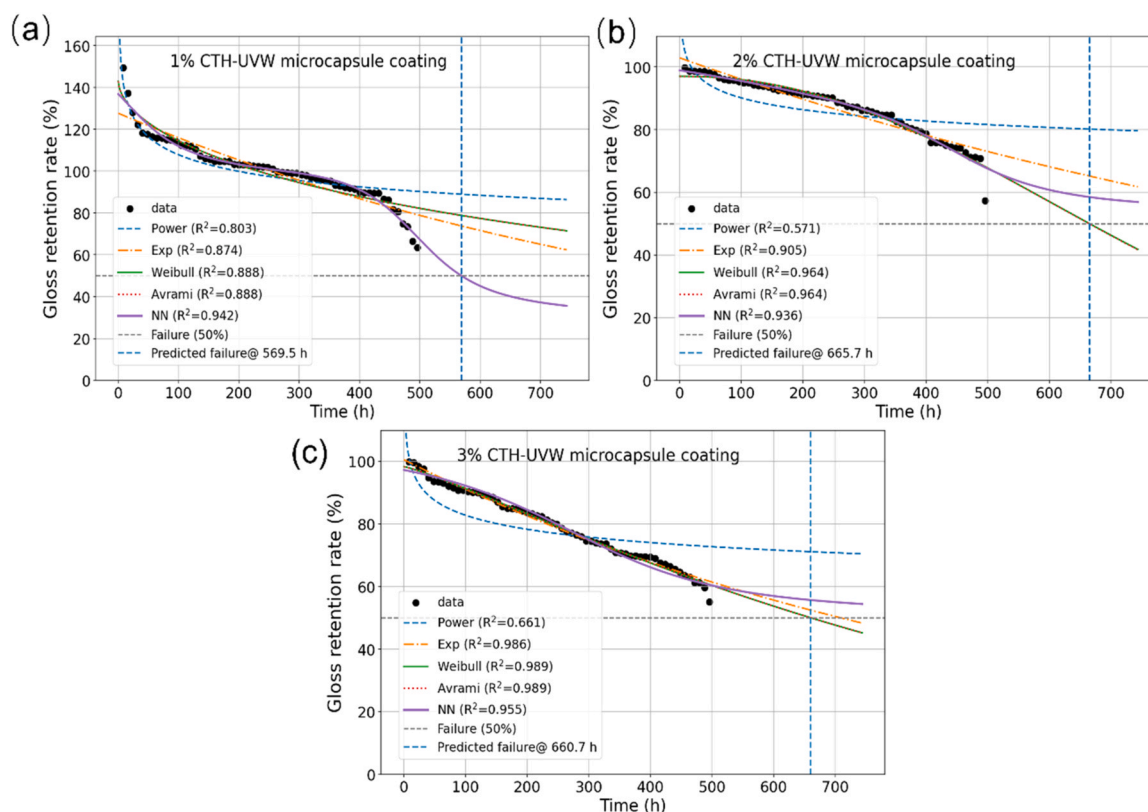


Fig. 6. Prediction of gloss life of CTH-W microcapsule UV coating : (a) 1.0% CTH-W microcapsule coating, (b) 2.0% CTH-W microcapsule coating, (c) 3.0% CTH-W microcapsule coating.



**Fig. 7.** Gloss lifespan of CTH-UVW microcapsule UV coating: (a) 1.0% CTH—UVW microcapsule UV coating, (b) 2.0% CTH—UVW microcapsule UV coating, (c) 3.0% CTH—UVW microcapsule UV coating.

which aligns well with the assumptions embedded in Weibull-type models. The scale and shape parameters of the Weibull function effectively capture the characteristic rate and acceleration of gloss loss, resulting in more stable extrapolation for lifetime prediction.

Color difference shows a clear plateau followed by an abrupt increase, implying a non-stationary aging response dominated by coupled, localized chemical events and threshold effects (e.g., delayed chromophore accumulation, oxidation “breakthrough”, or microcapsule-related migration/exudation). Such a “plateau-jump” pattern is difficult to represent with exponential or simple power-law forms that assume a smooth, time-invariant rate. The Avrami model can partially capture the induction-like stage and subsequent acceleration via time-dependent kinetics, whereas neural networks are generally more suitable because they can learn nonlinear interactions and regime transitions directly from the experimental data.

By contrast, gloss retention decreases rapidly at early times and then slows, consistent with cumulative and irreversible surface damage. The initial drop is mainly associated with rapid roughening and micro-defect/microcrack formation that increases light scattering, while the later deceleration reflects diffusion- or damage-limited evolution and partial saturation of scattering features. This monotonic “fast-then-slow” behavior is well described by physically interpretable parametric models: a power-law captures decelerating kinetics, and the Weibull model provides robust lifetime inference, with its shape and scale parameters reflecting the evolving degradation rate and characteristic timescale for gloss loss.

### 3.3. Thermal stability of UV coating

Fig. 8 presents the TGA and DTG curves of the UV coating and the coatings containing different types of microcapsules before and after 496 h of accelerated aging. As shown in Fig. 8(a), the pristine UV coating exhibited an initial decomposition temperature of 331 °C, with the

residual mass increasing slightly from 17.14% (before aging) to 19.14% (after aging), and a second DTG peak at 425 °C. This modest shift was consistent with limited aging-induced modification of the crosslinked polymer network, where partial scission/oxidation could have occurred while the overall thermal resistance remained largely retained. When 2.0% C-W microcapsules (WWO core) were incorporated (Fig. 8(b)), the second DTG peak shifted to 416 °C and, notably, the residual mass increased from 18.26% to 22.36% after aging. Given that WWO is dominated by long-chain aliphatic (partly unsaturated) fatty-acid derivatives that preferentially volatilize and yield little char upon heating, this residue increase was most plausibly attributed to aging-promoted release and/or oxidative depletion of the volatile core fraction during UV/hydrothermal exposure, which effectively reduced the proportion of thermally labile organics remaining in the coating and enriched the non-volatile fraction measured at high temperature. For the 2.0% CTH-W microcapsule coating (Fig. 8(c)), in which the same WWO core was combined with a chitosan/HPMC/TiO<sub>2</sub> hybrid shell, a higher residue was obtained before aging (23.35%), reflecting the inherently higher char-forming propensity of polysaccharide-based shells (chitosan and HPMC) together with the non-volatile contribution of TiO<sub>2</sub>. However, the residue decreased to 19.90% after aging, while the second DTG peak appeared at 422 °C. This decline suggested that, under prolonged UV/humidity exposure, the polysaccharide-rich shell and/or interfacial organics were more extensively degraded/eroded and/or converted into water-leachable low-molecular-weight products, thereby diminishing the amount of carbonaceous residue retained upon subsequent heating despite the presence of TiO<sub>2</sub>. In contrast, the CTH-UVW microcapsule coating (Fig. 8(d)) showed the highest and most stable high-temperature retention, with the residual mass increasing from 20.89% to 23.34% after aging and only a minor decomposition shift, indicating that the hybrid design (CTH shell combined with the UVW core) better preserved structural integrity during aging. The improved retention was attributed to the more constrained/denser organic phase created by UV curing of

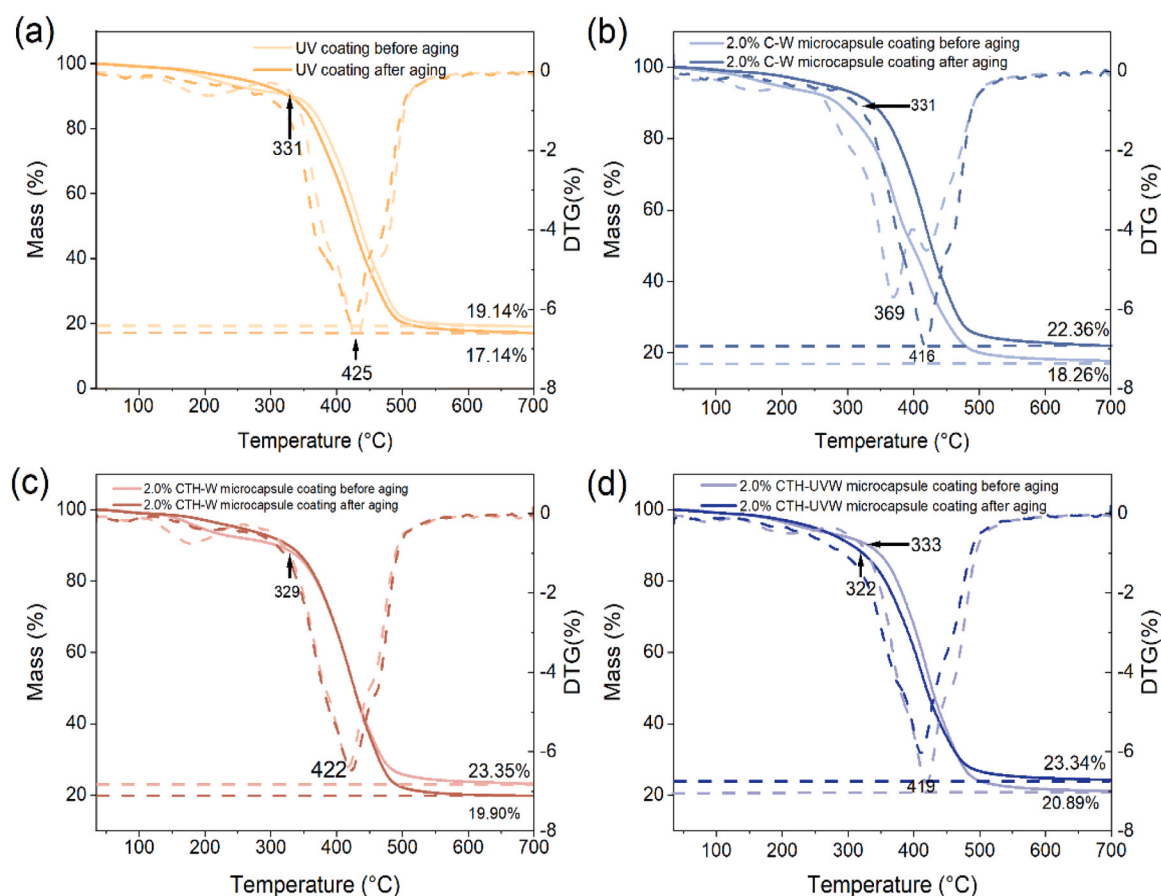


**Fig. 8.** TG and DTG analysis before and after coating aging: (a) UV coating aging, (b) C-W microcapsules coating, (c) CTH-W microcapsules coating, (d) CTH-UVW microcapsules coating.

the UVW core, which was expected to suppress extensive volatilization and migration of low-molecular-weight oil constituents during aging and to better preserve capsule integrity, thereby maintaining a larger non-volatile fraction (shell-derived char and  $\text{TiO}_2$ ) in the aged coating.

### 3.4. Microscopic analysis

Fig. 9 presents the SEM micrographs of UV coatings and microcapsule-modified coatings before and after aging. As shown in Fig. 9(a<sub>1</sub>), the unaged UV coating exhibits a relatively uniform and compact surface morphology with indistinct texture and no observable cracks or particle detachment. Minor micro-undulations are visible, but the overall surface remains smooth and intact. After 496 h of accelerated aging (Fig. 9(a<sub>2</sub>)), pronounced longitudinal cracks and groove-like structures appear, accompanied by a marked increase in surface roughness. These features are attributed to polymer embrittlement caused by ultraviolet degradation and thermo-oxidative reactions, indicating that microcracking and interlayer delamination occurred during the aging process.

In Fig. 9(b<sub>1</sub>), the unaged C-W microcapsule coating shows a rough and uneven surface with sparsely but uniformly distributed microcapsules. The coating retains good continuity without visible cracks. After aging, the overall morphology changes little (Fig. 9(b<sub>2</sub>)), particles remain discernible, and surface roughness slightly decreases. The absence of significant cracking suggests moderate resistance to aging, though the protective effect of this formulation is limited. The CTH-W microcapsule coating before aging (Fig. 9(c<sub>1</sub>)) exhibits a uniform yet slightly porous morphology with fine particulate features and relatively high roughness, possibly related to the CTH encapsulation structure. After aging (Fig. 9(c<sub>2</sub>)), the surface becomes smoother with diminished

particle texture, implying that microcapsules may have ruptured and merged with the polymer matrix during exposure. The absence of large cracks indicates a mild surface evolution process during aging. For the 2.0% CTH-UVW microcapsule coating (Fig. 9(d<sub>1</sub>)), the unaged surface shows a dense and compact morphology with finely dispersed particles and minimal porosity. The microcapsules are well embedded in the matrix, forming a smooth and continuous coating. After aging (Fig. 9(d<sub>2</sub>)), more distinct particle boundaries and protrusions appear, suggesting partial exposure of the capsule shells. The regular particle arrangement and preserved morphology indicate that this hybrid CTH-UVW system maintains good structural integrity and stability under aging conditions.

The FTIR spectra of the coatings before and after accelerated aging are presented in Fig. 10. The absorption at  $2933\text{ cm}^{-1}$  corresponds to the  $-\text{CH}_3/-\text{CH}_2$  stretching vibrations of UVW, while the  $582\text{ cm}^{-1}$  band is attributed to the Ti-O bond (Howell et al., 2001). In Fig. 10(a), the significant attenuation of the  $\text{C}=\text{O}$  ( $1776\text{ cm}^{-1}$ ),  $\text{C}-\text{O}-\text{C}$  ( $1060\text{ cm}^{-1}$ ), and  $\text{C}-\text{H}$  ( $2933/2854\text{ cm}^{-1}$ ) (Abdel-Hameed et al., 2025) peaks indicates structural degradation of the UV coating. For the C-W microcapsule coating (Fig. 10(b)), the intensity of the  $\text{C}-\text{H}$  band at  $2933\text{ cm}^{-1}$  decreases by approximately 77.5%, whereas the peaks at  $1776$  and  $1060\text{ cm}^{-1}$  increase. This enhancement is attributed to the partial rupture of the microcapsule wall, which releases WWO that undergoes oxidation under UV and atmospheric exposure, forming fatty acid esters, ketones, or peroxides. These carbonyl-containing oxidation products contribute to the intensified absorption near  $1776\text{ cm}^{-1}$ . As shown in Fig. 10(c), the CTH-W microcapsule coating exhibits a pronounced reduction in the characteristic absorptions at  $2933/2854\text{ cm}^{-1}$  ( $\text{C}-\text{H}$  stretching),  $\text{C}=\text{O}$  stretching ( $1776\text{ cm}^{-1}$ ), and  $\text{C}-\text{O}-\text{C}$  stretching ( $1060\text{ cm}^{-1}$ ) (Wu et al., 2019). The concurrent attenuation of these bands suggests that the



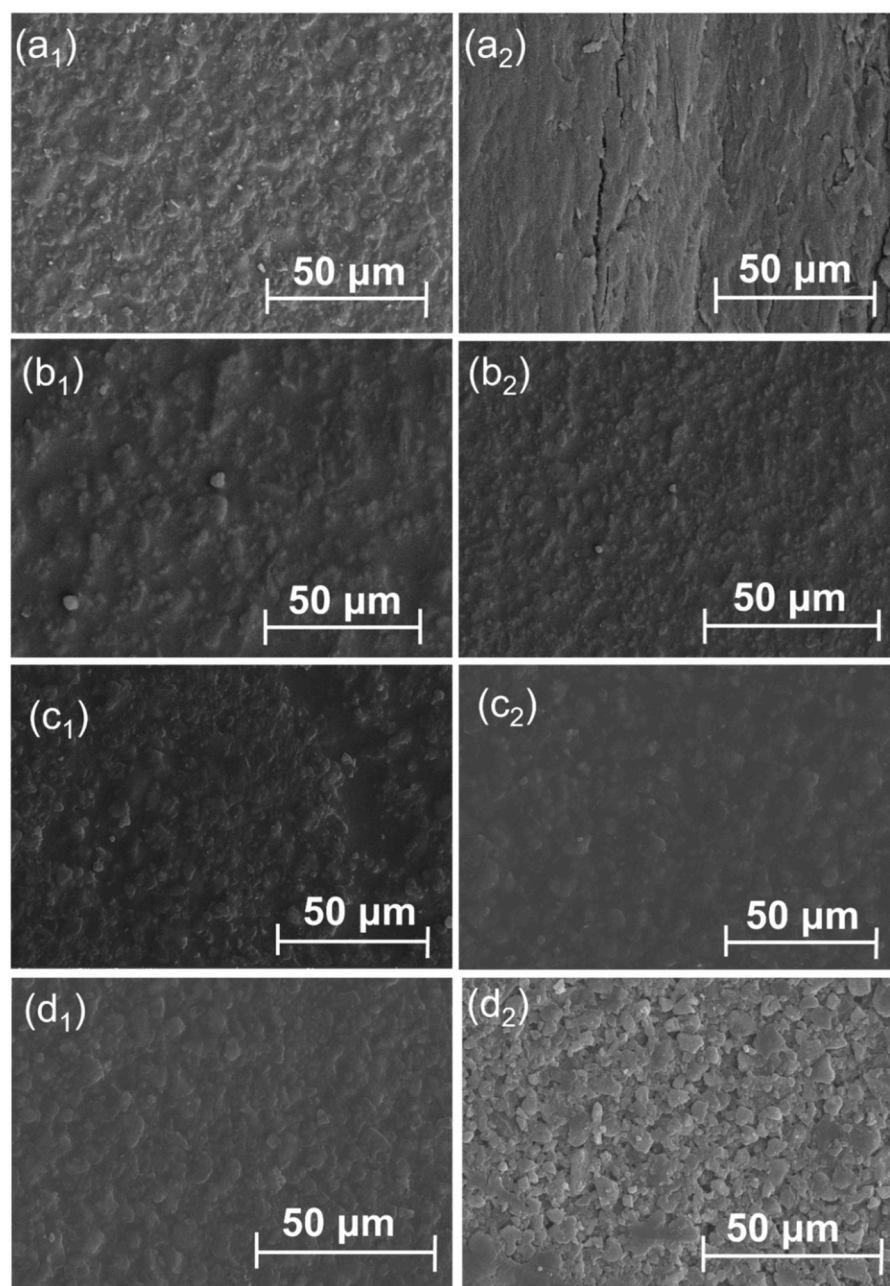


**Fig. 9.** SEM of microcapsule coating before and after aging: (a<sub>1</sub>) UV coating before aging, (a<sub>2</sub>) UV coating after aging, (b<sub>1</sub>) 2.0% C-W microcapsule coating before aging, (b<sub>2</sub>) 2.0% C-W microcapsule coating before aging, (c<sub>1</sub>) 2.0% CTH-W microcapsule coating before aging, (c<sub>2</sub>) 2.0% CTH-W microcapsule coating after aging, (d<sub>1</sub>) 2.0% CTH-UVW microcapsule coating before aging, (d<sub>2</sub>) 2.0% CTH-UVW microcapsule coating after aging.

original aliphatic and oxygen-containing functional groups were partially consumed or chemically transformed rather than simply eliminated. This evolution aligns with the mechanisms of photo-oxidation and thermal oxidation: (i) oxidation and chain scission of long alkyl chains weaken the C–H vibrations; (ii) cleavage or further oxidation of ester and ether groups modifies the C=O and C–O spectral features; and (iii) microcapsule rupture and release during aging promote migration or volatilization of organics from the coating surface, decreasing the local concentration of functional groups. Furthermore, the aging-induced crosslinking may lower vibrational freedom and apparent IR absorptivity, contributing to overall signal weakening. These mechanisms are consistent with complementary TGA/DTG and SEM results, which confirm oxidative degradation of the coating accompanied by partial release of the microcapsule core materials. In Fig. 10(d), the CTH-UVW microcapsule coating shows a marked

reduction of the bands at  $1776\text{ cm}^{-1}$  (C=O stretching),  $1060\text{ cm}^{-1}$  (C–O/C–O–C stretching) and  $2933\text{ cm}^{-1}$  (aliphatic C–H stretching). This simultaneous decrease is interpreted as a combined effect of oxidative degradation and physical migration, rather than a single degradation pathway. Under UV and hygrothermal exposure, photo- and thermo-oxidation accelerate chain scission and subsequent reactions of ester/ether and aliphatic moieties, thereby depleting the original functional groups and generating volatile low-molecular-weight fragments and oxidized species that contribute weakly in these regions. Additionally, the UVW core and its surrounding matrix may undergo further crosslinking during aging, which incorporates IR-active groups into a rigid, highly crosslinked network, effectively lowering their IR absorptivity. Partial rupture of microcapsules and migration or volatilization of released organics from the ATR sampling depth further diminish the surface signal intensity. Finally, the presence of  $\text{TiO}_2$  within

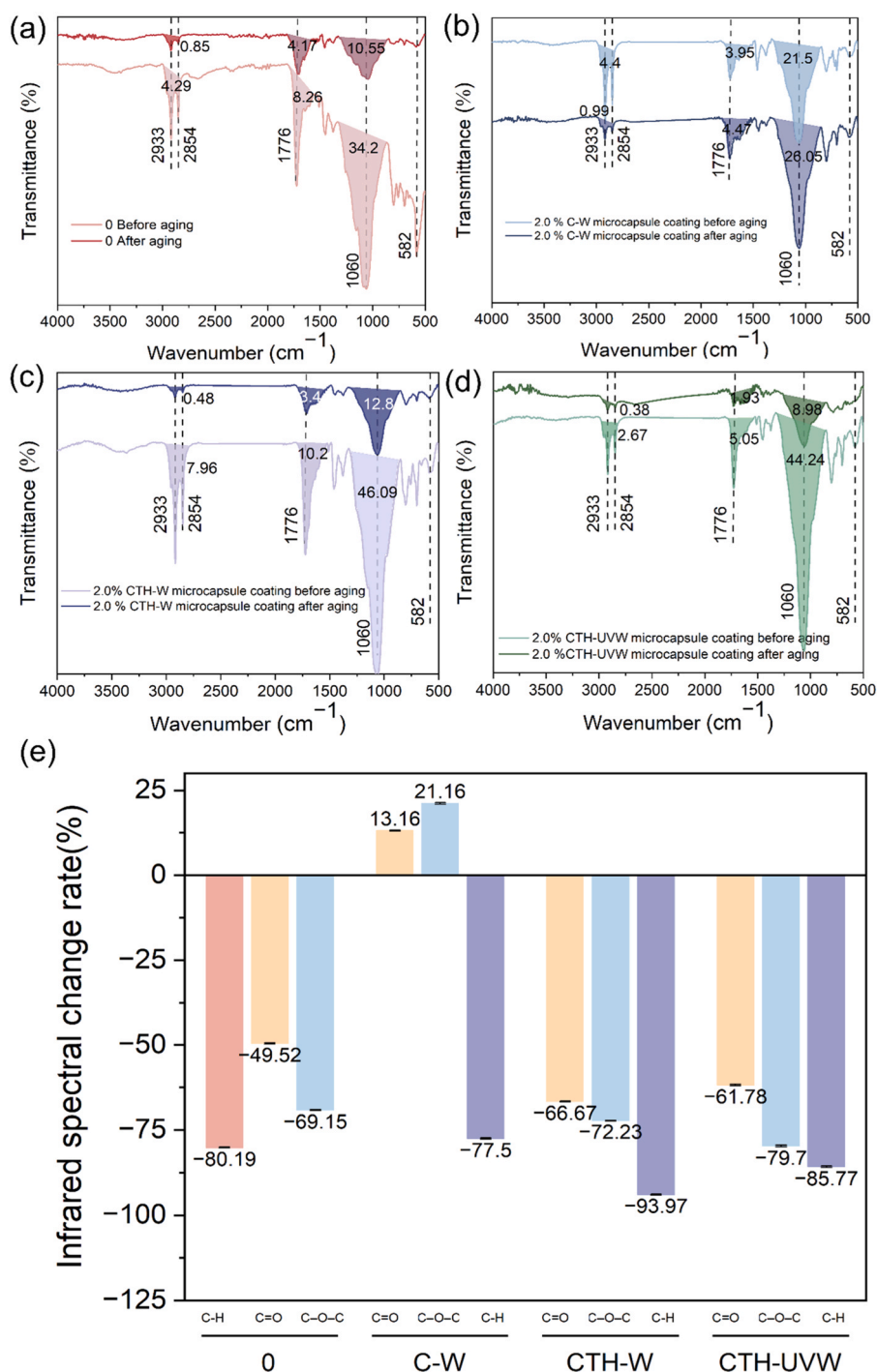


**Fig. 10.** Infrared spectra of coating before and after aging, (a)UV coating, (b)2.0% C-W microcapsule coating, (c)2.0% CTH-W microcapsule coating, (d) 2.0% CTH-UVW microcapsule coating. (e)Infrared spectral group change rate.

the CTH shell—and its potential photo-activity—may accelerate surface oxidation or mask organic absorptions by increasing the relative inorganic contribution. Collectively, these coupled processes account for the pronounced weakening of the 1776, 1060, and 2933  $\text{cm}^{-1}$  absorption bands, consistent with the SEM observations of microcapsule release and TGA evidence of reduced thermal residues, confirming the oxidative degradation and structural evolution of the coating system (Hu et al., 2025).

The relative variation in characteristic functional groups of the coatings before and after accelerated aging are illustrated in Fig. 10(e). For the pure UV coating, the C-H absorption decreased sharply from

4.29 to 0.85, representing an 80.19% reduction, indicating substantial degradation of hydrocarbon chains during aging. The C=O (carbonyl) group intensity decreased by 49.52%, likely due to photothermal cleavage or further oxidation of carbonyl functionalities. Meanwhile, the C-O-C ether linkage decreased significantly by 69.15%, suggesting structural instability. These results demonstrate that the pure UV coating underwent extensive degradation of alkyl, ether, and carbonyl groups, exhibiting poor aging resistance. For the C-W coating, C=O and C-O increase by 13.16% and 21.16%, respectively, while C-H decreases by 77.5%. This pattern reflects significant photo-oxidative scission of alkyl chains accompanied by the accumulation of oxygenated products,

corresponding to an intermediate oxidation stage dominated by oxygen-containing species build-up. In the CTH-W microcapsule coating, C=O decreases by 66.67%, C-O-C by 72.23%, and C-H by 93.97%, indicating drastic photo-/thermal-oxidative degradation. Both the backbone and side chains undergo extensive fragmentation, leading to depletion or

migration of oxygenated groups and hydrocarbons from the surface, consistent with surface embrittlement and functional deterioration. Although chitosan is present, the absence of UV curing results in a structurally unstable network with severe loss of chemical functionalities. For the CTH-UVW coating, the relative contents of C-H, C-O, and

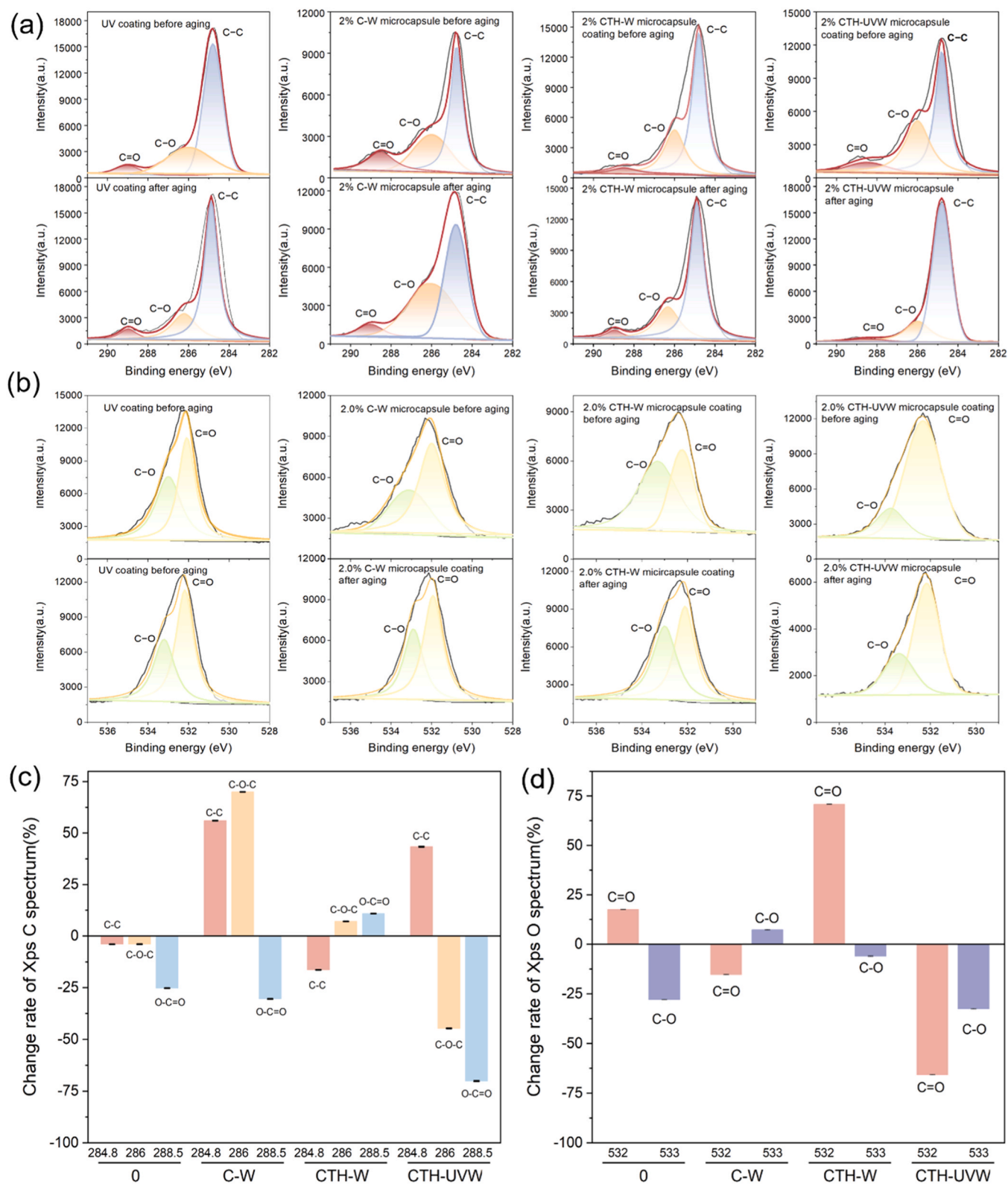


**Fig. 11.** XPS spectra of coatings before and after aging resistance: (a) XPS C spectrum, (b) XPS O spectrum, (c) Change rate of XPS C spectrum, (d) Change rate of XPS O spectrum.



C=O all decreased after aging. Specifically, C-H and C-O exhibited substantial reductions of 85.77% and 79.70%, respectively, whereas the C=O fraction decreased by 61.78%, which was less pronounced than in the neat and CTH-W coatings. The comparatively better preservation of C=O suggested that the combined effects of UV curing and the chitosan-containing microcapsule system improved the structural stability of carbonyl-bearing moieties. Overall, among all formulations, the CTH-UVW coating showed the highest resistance to aging. These trends were corroborated by ATR-FTIR analysis. After aging, the spectra displayed an overall decrease in absorbance at 2933 and 2854  $\text{cm}^{-1}$  (aliphatic  $-\text{CH}_2-$  stretching),  $\sim 1776 \text{ cm}^{-1}$  (carbonyl absorption), and 1442 and  $\sim 1060 \text{ cm}^{-1}$  (polysaccharide-framework-related C-H/C-O vibrations), while no pronounced band broadening or strong new shoulder features were observed in the carbonyl region. Considering that the system comprised chitosan as the microcapsule shell material together with hydroxypropyl methylcellulose (HPMC) and  $\text{TiO}_2$ , the spectral evolution was more consistent with depletion/erosion of surface organic constituents under UVW conditions than with accumulation of new oxidized functional groups at the surface. In particular,  $\text{TiO}_2$  was inferred to promote photocatalytic oxidative chain scission of the surface organic phase, and the condensation-wetting cycles were considered to enhance dissolution/leaching of low-molecular-weight oxidation products and other mobile organic fractions. Consequently, the apparent abundance of oxygen-containing organic functionalities (including C=O and C-O) within the ATR sampling depth was reduced. Consistent with this interpretation, XPS also showed decreased contributions of organic C=O and C-O components in the surface O 1s spectra, indicating that the post-aging surface became increasingly dominated by inorganic exposure and depleted in organic functional groups.

The XPS spectra of the UV coating and microcapsule-modified coatings before and after accelerated aging are presented in Fig. 11. Fig. 11(a) shows the C 1s spectra of the UV coating, and in combination with the variation ratios in Fig. 11(c), C=O decreases by 25.27%, while C-C and C-O decrease by 3.99% and 3.97%, respectively. These minor losses indicate that aging induces only mild oxidation, dominated by early-stage oxidative reactions and limited chain scission. For the 2.0 wt % C-W microcapsule coating, the intensities of C-C and C-O increase markedly after aging, suggesting surface enrichment of oxygen-containing functionalities and the occurrence of oxidative reactions. Meanwhile, the C=O peak becomes weaker, implying that the system possesses a certain degree of antioxidative or self-healing capability, resulting in a net decrease in the overall surface oxygen content. The increase in C-C bonding indicates carbon enrichment or deoxygenation, suggesting that the surface undergoes oxidative degradation followed by structural rearrangement and partial carbonization. This transition yields a more hydrophobic and chemically inert surface dominated by non-polar C-C/C-H linkages. The CTH-UVW microcapsule coating exhibits a different degradation trajectory: C-C increases sharply by 43.36%, whereas C-O and C=O decrease by 44.66% and 70.12%, respectively. The strong depletion of carbonyl-containing species indicates pronounced fragmentation or volatilization of molecular chains carrying C=O moieties. These compositional changes demonstrate a transition from the early oxidation-accumulation stage to an advanced oxidation-scission-volatilization stage, in which earlier-formed alcohol/ether and carbonyl species undergo secondary photolysis and escape as low-molecular-weight volatiles. Consequently, the surface becomes enriched in saturated, chemically inert carbon species. This transformation is accelerated by the synergistic effects of the  $\text{TiO}_2$ -containing CTH shell and the UV-curable polymer matrix. The resulting surface chemistry shifts toward a more highly cross-linked and less polar composition, consistent with the enhanced structural compactness and oxidative stability revealed by complementary FTIR and TGA analyses.

The O 1s XPS spectra is presented in Fig. 11(b), and Fig. 11(d) shows the corresponding change rates. In the UV coating, aging leads to an increase of 17.53% in the C=O component ( $\sim 532 \text{ eV}$ ), whereas the C-O

contribution decreases by 27.93%, indicating only mild oxidation accompanied by limited rearrangement of oxygenated species. For the C-W coating, the C=O component decreases by 15.32% while C-O increases by 7.28%. This trend suggests consumption or migration of carbonyl groups, along with the formation or exposure of additional alcohol/ether-type oxidation products and polyhydroxyl groups at the surface. The CTH-W coating exhibits a pronounced increase in C=O (+70.81%) and a reduction in C-O (−6.10%). These changes indicate a strong oxidation/chain-scission process, during which C-O linkages are further oxidized or cleaved to generate secondary carbonyl-containing products. The CTH-UVW coating shows a substantial decrease in both C=O (−65.69%) and C-O (−32.59%). This pattern implies that, after prolonged aging, the system evolves toward a more stabilized oxidized structure. Instead of continuing to accumulate new oxygenated functionalities, the coating undergoes intensive chain scission and subsequent migration or volatilization of oxidation products. The unsaturated components of the UVW initially oxidize rapidly to form low-molecular aldehydes, ketones, and acids. However, under sustained photo-thermal exposure, these species are further degraded and escape from the surface, resulting in an overall decrease in oxygen signals in the XPS spectra. This “deoxygenation” trend indicates a shift toward a more non-polar surface with increased exposure of the carbon backbone, suggesting embrittlement and interfacial instability during long-term aging. Although  $\text{TiO}_2$  contributes to short-term stability through its light-shielding effect, its photocatalytic activity under UV irradiation can generate reactive oxygen species ( $\cdot\text{OH}$ ,  $\text{O}_2\cdot^-$ ), which accelerate oxidative decomposition of the surrounding organic matrix, leading to adverse long-term effects.

Fig. 12(a) schematically illustrated the dominant aging pathways of the C-W and CTH-W microcapsule coatings after 62 cycles of UV irradiation coupled with high-humidity condensation. During aging, the unsaturated fatty-acid constituents in the WWO core were subjected to photooxidation and underwent hydroperoxide formation and subsequent decomposition. These processes were inferred to induce C=C bond cleavage and chain scission, thereby generating a range of polar oxidation products and low-molecular-weight fragments (e.g., short-chain mono- and dicarboxylic acids). The resulting species were considered likely to migrate, volatilize, and/or be removed by leaching under condensation water. Fig. 12(b) depicted the plausible reaction processes of the photoinitiating components in the CTH-UVW microcapsule coating under UV exposure. Specifically,  $\alpha$ -hydroxyketone structures were expected to undergo Norrish type I cleavage, producing benzoyl radicals and accompanying alkyl radicals, which subsequently initiated radical-mediated reactions. On the one hand, these radicals were considered capable of reacting with residual unsaturated bonds in the system and promoting further curing and densification; on the other hand, in the presence of  $\text{O}_2$  and water vapor, a certain degree of photooxidation and chain scission could also have occurred, leading to the formation of oxidized products such as carboxylic acids. Nevertheless, when the ATR-FTIR and XPS results were taken together, the post-aging surface signals associated with C=O, C-O, and aliphatic  $-\text{CH}_2-$  groups were found to decrease overall, and no pronounced band broadening or strong new shoulder features were observed in the carbonyl region. These observations more strongly supported a UVW-induced depletion/erosion of surface organic constituents accompanied by leaching removal of low-molecular-weight oxidation products, rather than sustained accumulation of oxidized species at the surface. This interpretation was consistent with the reduced contributions of organic C=O and C-O components in the XPS O 1s spectra, indicating that the aged coating surface became increasingly dominated by inorganic exposure and depleted in organic functional groups, which was considered beneficial for maintaining coating integrity and long-term self-healing performance.



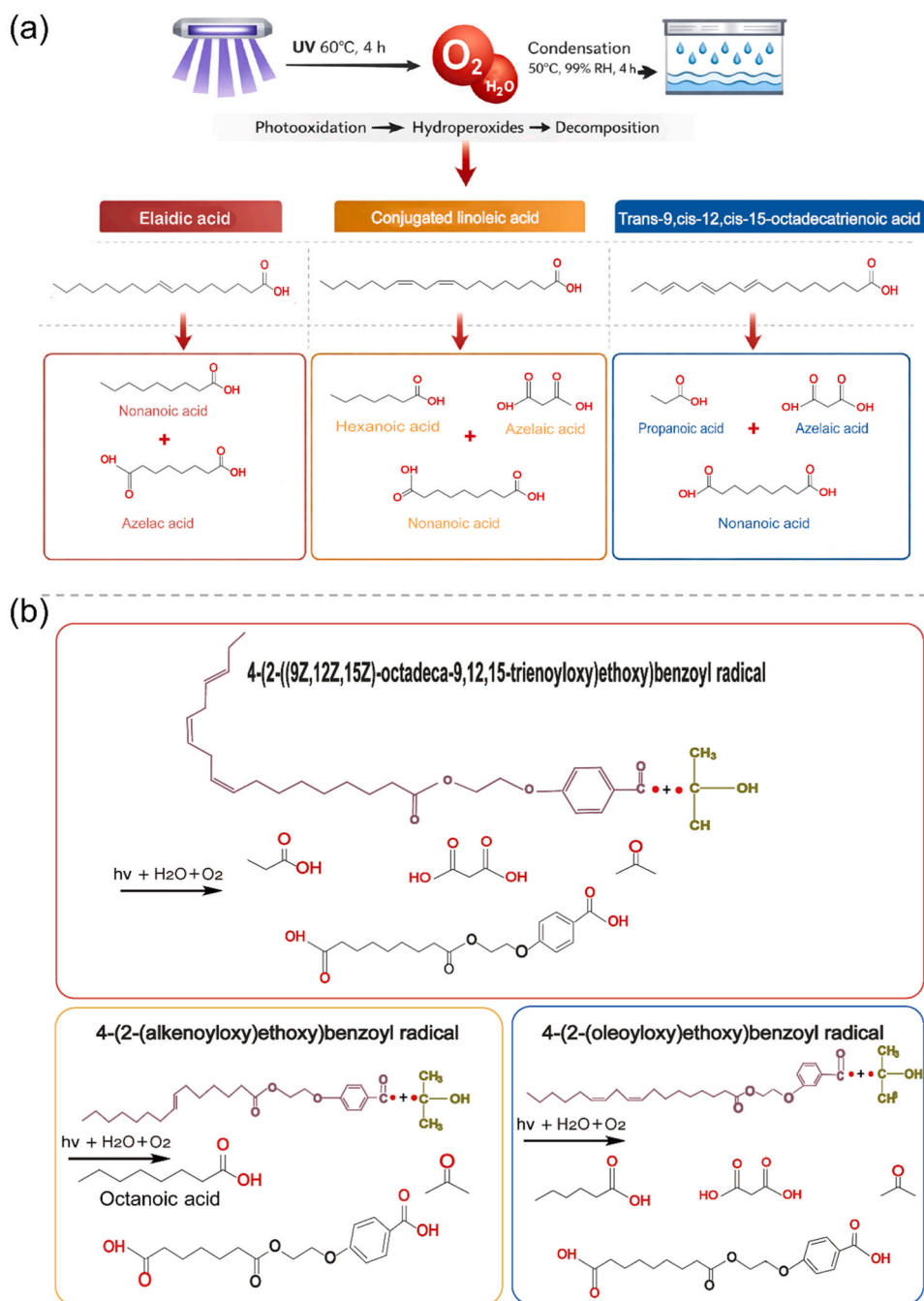


Fig. 12. Aging mechanism: (a) C-W microcapsule and CTH-W microcapsule (b) CTH-UVW microcapsule.

### 3.5. Aging adhesion

The aging-induced adhesion performance of the UV coating and the C-W microcapsule-modified coatings are compared in Fig. 13(a). The pristine UV coating exhibits a moderate initial adhesion strength, followed by a slight decline with prolonged aging. In contrast, the microcapsule-containing samples show pronounced fluctuations during the early stage (100–200 h). In particular, the 2.0% sample displays an abrupt increase to approximately 18 MPa at 100 h, followed by a sharp drop to a low and unstable level. The 3.0% sample shows a similar trend, albeit with a lower peak. The temporary increase in adhesion is likely associated with the thermal release and migration of the WWO core during the initial aging stage, which enhances interfacial wetting. Subsequent adhesion deterioration originates from chitosan shell cracking

and interfacial stress accumulation, indicating that the unmodified chitosan wall material provides limited long-term protection, as reflected by the overall instability of the C-W system. For Fig. 13(b), the samples exhibit higher initial adhesion strength—particularly the 2.0% and 3.0% formulations—suggesting that the incorporation of hydroxypropyl methylcellulose (HPMC) and  $TiO_2$  effectively reinforces interfacial bonding. However, adhesion strength decreases rapidly with aging and stabilizes after approximately 200 h. The diminishing differences among concentrations indicate that the system approaches a saturated failure state in the later stage of aging. Although the introduction of HPMC and  $TiO_2$  enhances shell compactness and UV-shielding capability, early improvements in adhesion cannot be sustained under alternating humid-thermal conditions. Migration of the WWO core eventually accelerates interfacial degradation, resulting in a

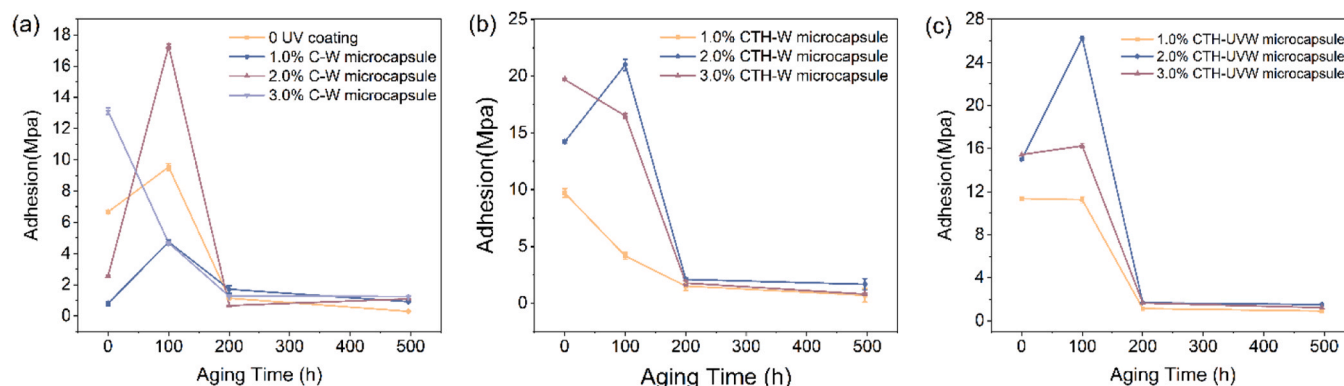


Fig. 13. (a) 0 and C-W microcapsule, (b) CTH-W microcapsule coating, (c) CTH-UVW microcapsule coating.

significant reduction in adhesion strength. Compared with Fig. 13(a), the CTH-W system displays improved stability, yet interfacial deterioration still occurs once the oil phase is released. Fig. 13(c) shows that the CTH-UVW microcapsules deliver the highest initial adhesion, with the 2.0% and 3.0% samples reaching 26.26 MPa and 16.25 MPa at 100–200 h, respectively, before declining sharply to below 2 MPa. The UVW core contains unsaturated groups and photo-initiators that facilitate partial crosslinking during early aging, thereby strengthening the coating–substrate interface. The subsequent decline is mainly attributed to surface embrittlement and thermo-oxidative degradation. Despite the substantial drop, the CTH-UVW system still outperforms the other two microcapsule formulations in both overall adhesion level and early-stage durability.

#### 4. Conclusions

After photo-thermal aging, the color-difference lifetime of the C-W microcapsule coating was 215.8 h. Incorporating 2.0% CTH-W microcapsules increased the lifetime to 337.8 h, while the 2.0% CTH-UVW microcapsule coating exhibited a remarkable extension to 1310.6 h. Among the prediction approaches, the neural-network model yielded the highest accuracy for chromaticity aging. Regarding gloss retention, the pure UV coating showed a lifetime of 359.1 h, the C-W microcapsule coating is 493.6 h, the CTH-W formulation increased this value to 569.5 h, and the CTH-UVW coating further improved it to 665.7 h. In this case, the Weibull model provided the most reliable lifetime prediction. Mass-loss and thermogravimetric displacement analyses before and after aging revealed that the CTH-UVW coating maintained the highest residual mass and the smallest thermal-decomposition displacement. SEM observations showed pronounced cracking only in the pure UV coating, whereas the other systems exhibited minimal morphological degradation. FTIR changes were also smallest in the CTH-UVW coating, indicating the lowest degree of oxidation and chain scission, thus confirming the strongest aging stability. The overall aging-resistance ranking was CTH-UVW microcapsule coating > CTH-W microcapsule coating > C-W microcapsule coating. The superior performance of the CTH-UVW system arises from the synergistic effects of the UVW crosslinked network, the enhanced shell compactness imparted by HPMC, and the UV-shielding capability of TiO<sub>2</sub>, collectively enabling outstanding short- and mid-term durability. The CTH-W formulation exhibited moderate performance, whereas the C-W coating showed the poorest stability due to the degradable nature of chitosan and the rapid oxidation of conventional wood wax oil. Even after aging, the 2.0% CTH-UVW microcapsule coating retained the highest adhesion rating, further demonstrating its superior structural integrity compared with other systems. Overall, the CTH-UVW microcapsule coating exhibits the most promising long-term aging resistance, combining excellent chemical stability, interfacial robustness, and weatherability, and represents the coating configuration with the greatest engineering application

potential within this study.

#### CRediT authorship contribution statement

**Zhihui Wu:** Writing – review & editing, Supervision, Resources, Investigation, Funding acquisition, Conceptualization. **Yijuan Chang:** Writing – review & editing, Writing – original draft, Software, Methodology, Investigation, Funding acquisition, Formal analysis, Data curation. **Jinxin Wang:** Writing – original draft, Visualization, Formal analysis, Data curation.

#### Declaration of Generative AI and AI-assisted technologies in the writing process

During the preparation of this work the author(s) used [Chatgpt] in order to improve language and readability. After using this tool, we reviewed and edited the content as needed and take(s) full responsibility for the content of the publication.

#### Funding

This work was funded by the National Key Research and Development Program (nos. 2016YFD0600704, 2018YFD0600304, and 2023YFD2201501) and the Graduate Research and Practice Innovation Program of Jiangsu Province (grant no. KYCX23\_1195).

#### Declaration of Competing Interest

The author declared that they have no conflicts of interest to this work. We declare that we do not have any commercial or associative interest that represents a conflict of interest in connection with the work submitted.

#### Data availability

Data will be made available on request.

#### References

- Abdel-Hameed, R., Ashmawy, A., Abourashed, N.M., Hegazy, A., Huwaimel, B., Fargally, O., Ali, A.A., Tantawy, A.H., Mohamed, H.I., 2025. Ionic liquid-based cationic gemini surfactants with polymeric spacer as inducers for Cu<sub>2</sub>O nanoparticles production: green synthesis, characterization, and surface activity. *J. Mol. Liq.* 426, 127306.
- Bekas, D.G., Tsirka, K., Baltzis, D., Paipetis, A.S., 2016. Self-healing materials: a review of advances in materials, evaluation, characterization and monitoring techniques. *Compos. Part B Eng.* 87, 92–119.
- Bloomfield, P., 1973. An exponential model for the spectrum of a scalar time series. *Biometrika* 60, 217–226.
- Busso, E.P., Wright, L., Evans, H.E., McCartney, L.N., Saunders, S.R.J., Osgerby, S., Nunn, J., 2007. A physics-based life prediction methodology for thermal barrier coating systems. *Acta Mater.* 55, 1491–1503.

- Chang, Y., Liu, E., Wu, Z., 2025. Constructing chitosan microcapsules using hydroxypropyl methylcellulose for self-healing antibacterial wood coating. *Int. J. Biol. Macromol.* 308, 142300.
- Chang, Y., Wu, Z., Liu, E., 2024. Fabrication of chitosan-encapsulated microcapsules containing wood wax oil for antibacterial self-healing wood coatings. *Ind. Crops Prod.* 222, 119438.
- Chang, Y., Wu, Z., 2024. Synthesized high performance UV-cured wood wax oil using Irgacure 2959 modified thistle oil and linseed oil. *Ind. Crops Prod.* 218, 118952.
- Chen, Y., Liu, R., Luo, J., 2022. Enhancing weathering resistance of UV-curable coatings by using TiO<sub>2</sub> particles as filler. *Prog. Org. Coat.* 169, 106936.
- Clauset, A., Shalizi, C.R., Newman, M.E.J., 2009. Power-law distributions in empirical data. *SIAM Rev.* 51, 661–703.
- Coronel-Aguilera, C.P., San Martín-González, M.F., 2015. Encapsulation of spray dried  $\beta$ -carotene emulsion by fluidized bed coating technology. *LWT Food Sci. Technol.* 62, 187–193.
- Croll, S., Hinderliter, B., 2008. A framework for predicting the service lifetime of composite polymeric coatings. *J. Mater. Sci.* 43, 6630–6641.
- Deng, J., Huang, N., Yan, X., 2023. Effect of composite addition of antibacterial/ photochromic/self-repairing microcapsules on the performance of coatings for medium-density fiberboard. *Coatings* 13, 1880.
- Dong, Y., Deng, J., Yan, X., 2025a. Effect of chitosan gum arabic-coated tung oil microcapsules on the performance of uv coating on cherry wood surface. *Coatings* 15.
- Dong, Y., Deng, J., Yan, X., 2025b. Preparation of tung oil microcapsules coated with chitosan sodium triphosphate and their effects on coating film properties. *Coatings* 15.
- Feng, X., Wang, Q., Yang, Z., Liu, X., 2025. Kinetics analysis of radical photopolymerizations for UV-curable nanocomposites based on cellulose nanocrystals: promoting and enhancing mechanisms. *Int. J. Biol. Macromol.* 287, 138700.
- Gan, J., Lin, Q., Huang, Y., Wu, Y., Yu, W., 2023. Full-Wood Utilization Strategy toward a Directional Luminescent Solar Concentrator. *ACS Nano* 17, 23512–23523.
- Gribova, V., Navalikhina, A., Lysenko, O., Calligaro, C., Lebaudy, E., Deiber, L., Senger, B., Lavalle, P., Vrana, N.E., 2021. Prediction of coating thickness for polyelectrolyte multilayers via machine learning. *Sci. Rep.* 11, 18702.
- Han, W., Wang, M., Yang, Y., Yao, H., Zhang, W., Hu, L., Huang, J., 2025. Preparation of efficiently anti-fungal and hydrophobic coatings using lignin@clove essential oil based microcapsules. *Ind. Crops Prod.* 226, 120711.
- Howell, N.K., Herman, H., Li-Chan, E.C.Y., 2001. Elucidation of protein–lipid interactions in a lysozyme–corn oil system by fourier transform raman spectroscopy. *J. Agric. Food Chem.* 49, 1529–1533.
- Hu, Y., Wan, Z., Song, H., Jiang, F., Liu, X., Liu, C., Xu, J., Liu, P., 2025. Ultralong cycle stability poly(benzodifurandione)/Ti<sub>3</sub>C<sub>2</sub>Tx films as novel self-supporting electrodes for supercapacitors. *J. Energy Storage* 135, 118279.
- Jonas, J.J., Quelennec, X., Jiang, L., Martin, É., 2009. The Avrami kinetics of dynamic recrystallization. *Acta Mater.* 57, 2748–2756.
- Kriegeskorte, N., Golan, T., 2019. Neural network models and deep learning. *Curr. Biol.* 29, R231–R236.
- Li, H., Cui, Y., Li, Z., Zhu, Y., Wang, H., 2018. Fabrication of microcapsules containing dual-functional tung oil and properties suitable for self-healing and self-lubricating coatings. *Prog. Org. Coat.* 115, 164–171.
- Li, N., Lei, Y., Lin, J., Ding, S.X., 2015. An Improved Exponential Model for Predicting Remaining Useful Life of Rolling Element Bearings. *IEEE Trans. Ind. Electron.* 62, 7762–7773.
- Li, P., Wu, X., Grosu, R., Hou, J., Ilolov, M., Xiang, S., 2025. Applying neural network to health estimation and lifetime prediction of lithium-ion batteries. *IEEE Trans. Transp. Electrification* 11, 4224–4248.
- Lin, W., Zhao, Y., Edwards, G., Guo, Q., Chen, T., Song, S., Heitzmann, M., Martin, D., Grøndahl, L., Lu, M., Huang, H., 2024. Mechanical properties and scratch recovery of nanoclay/polyester composite coatings for pre-coated metal (PCM) sheets. *Compos. Part B Eng.* 273, 111217.
- Lux, T., Alfarano, S., 2016. Financial power laws: empirical evidence, models, and mechanisms. *Chaos Solitons Fractals* 88, 3–18.
- Prabhakar Murthy, D.N., Bulmer, M., Eccleston, J.A., 2004. Weibull model selection for reliability modelling. *Reliab. Eng. Syst. Saf.* 86, 257–267.
- Shirzad, K., Viney, C., 2023. A critical review on applications of the Avrami equation beyond materials science. *J. R. Soc. Interface* 20, 20230242.
- Slot, H.M., Gelinck, E.R.M., Rentrop, C., van der Heide, E., 2015. Leading edge erosion of coated wind turbine blades: Review of coating life models. *Renew. Energy* 80, 837–848.
- Smith, R.L., 1991. Weibull regression models for reliability data. *Reliab. Eng. Syst. Saf.* 34, 55–76.
- Šuštersiĉ, T., Gribova, V., Nikolic, M., Lavalle, P., Filipovic, N., Vrana, N.E., 2023. The effect of machine learning algorithms on the prediction of layer-by-layer coating properties. *ACS Omega* 8, 4677–4686.
- Taskinen, J., Yliruusi, J., 2003. Prediction of physicochemical properties based on neural network modelling. *Adv. Drug Deliv. Rev.* 55, 1163–1183.
- Traeger, F., Ahrens, M., Vaßen, R., Stöver, D., 2003. A life time model for ceramic thermal barrier coatings. *Mater. Sci. Eng. A* 358, 255–265.
- Wais, P., 2017. A review of Weibull functions in wind sector. *Renew. Sustain. Energy Rev.* 70, 1099–1107.
- Wang, Q., Yang, Z., Feng, X., Liu, X., 2023. Modification of nanocellulose via atom transfer radical polymerization and its reinforcing effect in waterborne UV-curable resin. *Int. J. Biol. Macromol.* 253, 126743.
- Wang, Q., Yang, Z., Liu, X., Feng, X., 2026. Construction of wood coatings based on nanocellulose photocurable composites and their enhancement mechanisms. *Prog. Org. Coat.* 211, 109820.
- Wu, Y., Wu, X., Shi, T., Chen, H., Wang, H., Sun, M., Zhang, J., 2019. The microstructure and mechanical properties of poplar catkin fibers evaluated by atomic force microscope (AFM) and nanoindentation. *Forests* 10.
- Wu, Y., Zhou, J., Huang, Q., Yang, F., Wang, Y., Wang, J., 2020. Study on the properties of partially transparent wood under different delignification processes. *Polymers*.
- Zhou, J., Xu, W., 2024. A fast method to prepare highly isotropic and optically adjustable transparent wood-based composites based on interface optimization. *Ind. Crops Prod.* 218, 118898.